Draft version September 21, 2015
Preprint typeset using LaTeX style emulateapj v. 12/16/11

ACTION-BASED DYNAMICAL MODELLING OF THE MILKY WAY DISK WITH *ROADMAPPING* AND OUR IMPERFECT KNOWLEDGE OF THE "REAL WORLD"

Wilma H. Trick[1,2], Jo Bovy[3], and Hans-Walter Rix[1]

Draft version September 21, 2015

ABSTRACT

We present *RoadMapping*, a dynamical modelling machinery that aims to recover the Milky Way's (MW) gravitational potential and the orbit distribution of stellar populations in the Galactic disk. *RoadMapping* is a full likelihood analysis that models the observed positions and velocities of stars with an equilibrium, three-integral distribution function (DF) in an axisymmetric potential. In preparation for the application to the large data sets of modern surveys like Gaia, we create and analyze a large suite of mock data sets and develop qualitative "rules of thumb" for which characteristics and limitations of data, model and machinery affect constraints on the potential and DF most. We find that, while the precision of the recovery increases with the number of stars, the numerical accuracy of the likelihood normalisation becomes increasingly important and dominates the computational efforts. The modelling has to account for the survey's selection function, but *RoadMapping* seems to be very robust against small misjudgments of the data completeness. Large radial and vertical coverage of the survey volume gives in general the tightest constraints. But no observation volume of special shape or position and stellar population should be clearly preferred, as there seem to be no stars that are on manifestly more diagnostic orbits. We propose a simple approximation to include measurement errors at comparably low computational cost that works well if the distance error is $\lesssim$ 10%. The model parameter recovery is also still possible, if the proper motion errors are known to within 10% and are $\lesssim 2$ mas yr^{-1}. We also investigate how small deviations of the stars' distribution from the assumed DF influence the modelling: An over-abundance of high velocity stars affects the potential recovery more strongly than an under-estimation of the DF's low-velocity domain. Selecting stellar populations according to mono-abundance bins of finite size can give reliable modelling results, as long as the DF parameters of two neighbouring bins do not vary more than 20% [TO DO: CKECK]. As the modelling has to assume a parametric form for the gravitational potential, deviations from the true potential have to be expected. We find, that in the axisymmetric case we can still hope to find a potential that is indeed a reliable best fit within the limitations of the assumed potential. Overall *RoadMapping* works as a reliable and unbiased estimator, and is robust against small deviations between model and the "real world".

Keywords: Galaxy: disk — Galaxy: fundamental parameters — Galaxy: kinematics and dynamics — Galaxy: structure

1. INTRODUCTION

Stellar dynamical modelling can be employed to infer the Milky Way's gravitational potential from the positions and motions of individual stars (Binney & Tremaine 2008; Binney 2011; Rix & Bovy 2013). Observational information on the 6D phase-space coordinates of stars is currently growing at a rapid pace, and will be taken to a whole new level in number and precision by the upcoming data from the Gaia mission (Perryman et al. 2001). Yet, rigorous and practical modelling tools that turn position-velocity data of individual stars into constraints both on the gravitational potential and on the distribution function (DF) of stellar orbits, are scarce (Rix & Bovy 2013) [TO DO: more references] [TO DO: References that explain that the modelling is scarce, or previous modelling approaches???] [TO DO: Hans-Walter suggested a Sanders & Binney reference, but I'm still not sure to what kind of paper: modelling approach or review of scarce modelling tools...]

The Galactic gravitational potential is fundamental for understanding the Milky Way's dark matter and baryonic structure (Rix & Bovy 2013; McMillan 2012; Strigari 2013; Read 2014) and the stellar-population dependent orbit distribution function is a basic constraint on the Galaxy's formation history (Binney 2013; Rix & Bovy 2013; Sanders & Binney 2015) [TO DO: more references].

There is a variety of practical approaches to dynamical modelling of discrete collisionless tracers, such as the stars in the Milky Way (e.g. Jeans modelling: Kuijken & Gilmore (1989), Bovy & Tremaine (2012), Garbari et al. (2012), Zhang et al. (2013), Büdenbender et al. (2015); action-based DF modelling: Bovy & Rix (2013), Piffl et al. (2014), Sanders & Binney (2015); torus modelling: McMillan & Binney (2012, 2013); Made-to-measure modelling: Syer & Tremaine (1996), de Lorenzi et al. (2007) or Hunt & Kawata (2014). Most of them – explicitly or implicitly – describe

[1] Max-Planck-Institut für Astronomie, Königstuhl 17, D-69117 Heidelberg, Germany
[2] Correspondence should be addressed to trick@mpia.de.
[3] University of Toronto [TO DO: What is Jo's current adress???]

the stellar distribution through a distribution function.

Actions are good ways to describe orbits, because they are canonical variables with their corresponding angles, have immediate physical meaning, and obey adiabatic invariance (Binney & Tremaine 2008; McMillan & Binney 2008; Binney 2010; Binney & McMillan 2011; Binney 2011). Recently, Binney (2012) and Bovy & Rix (2013) [TO DO: are these the correct references???] proposed to combine parametrized axisymmetric potentials with DF's that are simple analytic functions of the three orbital actions to model discrete data. Binney (2010) and Binney & McMillan (2011) had proposed a set of simple action-based (quasi-isothermal) distribution functions (qDF). Ting et al. (2013) and Bovy & Rix (2013) showed that these qDF's may be good descriptions of the Galactic disk, when one only considers so-called mono-abundance populations (MAP), i.e. sub-sets of stars with similar [Fe/H] and [α/Fe] (Bovy et al. 2012b,c,d).

Bovy & Rix (2013) implemented a rigorous modelling approach that put action-based DF modelling of the Galactic disk in an axisymmetric potential in practice. Given an assumed potential and an assumed DF, they directly calculated the likelihood of the observed $(\vec{x},\vec{v})$ for each sub-set of MAP among SEGUE G-dwarf stars (Yanny et al. 2009). This modelling also accounted for the complex, but known selection function of the kinematic tracers. For each MAP, the modelling resulted in a constraint of its DF, and an independent constraint on the gravitational potential, which members of all MAPs feel the same way.
Taken as an ensemble, the individual MAP models constrained the disk surface mass density over a wide range of radii ($\sim 4-9$ kpc), and proved a powerful constraint on the disk mass scale length and on the disk-to-dark-matter ratio at the Solar radius.

Yet, these recent models still leave us poorly prepared with the wealth and quality of the existing and upcoming data sets. This is because Bovy & Rix (2013) made a number of quite severe and idealizing assumptions about the potential, the DF and the knowledge of observational effects (such as the selection function). All these idealizations are likely to translate into systematic error on the inferred potential or DF, well above the formal error bars of the upcoming data sets.

In this work we present *RoadMapping* ("Recovery of the Orbit Action Distribution of Mono-Abundance Populations and Potential INference for our Galaxy") - an improved and refined version of the original dynamical modelling machinery by Bovy & Rix (2013), making extensive use of the *galpy* Python package (Bovy 2015) and the *Stäckel Fudge* for fast action calculations by Binney (2012). *RoadMapping* is robust and well-tested and explicitly developed to exploit and deal with the large data sets of the future. *RoadMapping* explores and relaxes some of the restraining assumptions that Bovy & Rix (2013) made and is more flexible and more adept in dealing with large data sets. In this paper we set out to explore the robustness of *RoadMapping* against the breakdowns of some of the most important assumptions of DF-based dynamical modelling. Our goal is to examine which aspects of the data, the model and the machinery itself limit our recovery of the true gravitational potential.

In the light of the imminent Gaia data, we analyze how well *RoadMapping* behaves in the limit of large data. For a huge number of stars three aspects become important, that may be hidden behind Poisson noise for smaller data sets: (i) We have to make sure that *RoadMapping* is an unbiased estimator (Section 3.1). (ii) Numerical inaccuracies in the actual modelling machinery must not be an important source of systematics (Section 2.6). (iii) As parameter estimates become much more precise (Section 3.1, we need more flexibility in the potential and DF model. The modelling machinery therefore has to effective in finding the best fit parameters for a large set of free model parameters. The improvements made in *RoadMapping* as compared to the machinery used in Bovy & Rix (2013) are presented in Section 2.7.

We also explore how different aspects of the observational experiment design impact the parameter recovery. (i) In an era where we can choose data from different MW surveys, it might be worth to explore the importance of the survey volume geometry, size and shape, and if different regions within the MW might be especially diagnostic to constrain the potential (Section 3.2). (ii) What if our knowledge of the sample selection function is imperfect, and potentially biased (Section 3.3)? (iii) How to best account for individual measurement errors in the modelling (Section 3.4)?

One of the strongest assumptions is to restrict the dynamical modelling to a certain family of parametrized models. We investigate how well we can we hope to recover the true potential, when our potential and DF models do not encompass the true potential and DF. First, we examine in Section 3.5 what would happen if the stars within MAPs do intrinsically not follow a single qDF as assumed by Ting et al. (2013) and Bovy & Rix (2013). Second, we test in Section 3.6 how well the modelling works, if our assumed potential family deviaties from the true potential.

The strongest assumption that goes into this kind of dynamical modelling might be the idealization of the Galaxy to be axi-symmetric and being in steady state. We do not investigate this within the scope of this paper but strongly suggest a systematic investigation of this for future work.

For all of the above aspects we show some plausible and illustrative examples on the basis of investigating mock data. The mock data is generated from galaxy models presented in Sections 2.1-2.4 following the procedure in Section 2.5, analysed according to the description of the *RoadMapping* machinery in Sections 2.6-2.7 and the results are presented in Section 3 and discussed in Section 4.

[TO DO: Comment from Hans-Walter: Make sure, any topic/issue appears only once]
[TO DO: Is now one quarter shorter than before. But maybe shorten it even more...]

[TO DO: Comment from Hans-Walter: Make clear "new in this paper", "general background", "exactly as in BR13"]

2. DYNAMICAL MODELLING

[TO DO: HW: In this section you have to indicate somehow, where you recapitulate BR13 and what is added new. "as in BR13", "beyond BR13"] TO DO: Comment from Hans-Walter: Basics of the method (binney, BR13) can be dramatically shortened. No need to sing the praises of
DF's and actions.

In this section we summarize the basic elements of *RoadMapping*, the dynamical modelling machinery presented in this work, which in many respects follows Bovy & Rix (2013).

2.1. *Coordinate System*

Our modelling takes place in the Galactocentric rest-frame with cylindrical coordinates $\boldsymbol{x} \equiv (R, \phi, z)$ and corresponding velocity components $\boldsymbol{v} \equiv (v_R, v_\phi, v_z)$. If the stellar phase-space data is given in observed heliocentric coordinates, position $\tilde{\boldsymbol{x}} \equiv (\mathrm{RA}, \mathrm{DEC}, m - M)$ in right ascension RA, declination DEC and distance modulus $(m - M)$ as proxy for the distance from the sun, and velocity $\tilde{\boldsymbol{v}} \equiv (\mu_{\mathrm{RA}}, \mu_{\mathrm{DEC}}, v_{\mathrm{los}})$ as proper motions $\boldsymbol{\mu} = (\mu_{\mathrm{RA}}, \mu_{\mathrm{DEC}})$ [TO DO: cos somwhere???] in both RA and DEC direction and line-of-sight velocity v_{los}, the data $(\tilde{\boldsymbol{x}}, \tilde{\boldsymbol{v}})$ has to be converted first into the Galactocentric rest-frame coordinates $(\boldsymbol{x}, \boldsymbol{v})$ using the sun's position and velocity. We assume for the sun

$$(R_\odot, \phi_\odot, z_\odot) = (8 \text{ kpc}, 0^\circ, 0 \text{ kpc})$$
$$(v_{R,\odot}, v_{T,\odot}, v_{z,\odot}) = (0, 230, 0) \text{ km s}^{-1}.$$

2.2. *Actions and Potential Models*

Orbits in axisymmetric potentials are best described and fully specified by the three actions $\boldsymbol{J} \equiv (J_R, J_z, J_\phi = L_z)$, defined as

$$J_i = \frac{1}{2\pi} \oint_{\mathrm{orbit}} p_i \, \mathrm{d}x_i, \qquad (1)$$

and which depend on the potential via the connection between position x_i and momentum p_i along the orbit. Actions have a clear physical meaning: They quantify the amount of oscillation in each coordinate direction of the full orbit [TO DO: REF: HW suggested Binney & Tremaine (2008), but I can't find a corresponding statement in the book]. The position of a star along the orbit is denoted by a set of angles, which form together with the angles a set of canonical conjugate phase-space coordinates (Binney & Tremaine 2008, §3.5.1).

Even though actions are excellent orbit labels and arguments for stellar distribution functions, their computation is typically very expensive and depends on the choice of potential in which the star moves. The spherical isochrone potential (Henon 1959) is the only [TO DO: Jo suggested "most general Galactic" instead of "only", but the isochrone is actually not Galactic... Ask him.] potential for which Equation 1 takes an analytic form (Binney & Tremaine 2008, §3.5.2). For Stäckel potentials actions can be calculated exactly by the (numerical) evaluation of a single integral. In all other potentials numerically calculated actions will always be approximations, unless Equation 1 is integrated along the whole (often not periodic) orbit. A computational fast way to get actions for arbitrary axisymmetric potentials is the *Stäckel fudge* by Binney (2012), which locally approximates the potential by a Stäckel potential. To speed up the calculation even more, an interpolation grid for J_R and J_z in energy E, angular momentum L_z and [TO DO: what else???] can be build out of these Stäckel fudge actions, as described in Bovy (2015).

For the gravitational potential in our modelling we assume a family of parametrized potential models with a fixed number of free parameters. We use different kinds of potentials: The Milky Way like potential from Bovy & Rix (2013) (`MW13-Pot`) with bulge, disk and halo; the spherical isochrone potential (`Iso-Pot`) in our test suites to make use of the analytic (and therefore exact and fast) way to calculate actions; and the 2-component Kuzmin-Kutuzov Stäckel potential (Batsleer & Dejonghe 1994; `KKS-Pot`), which displays a disk and halo structure and also provides exact actions. Table 1 summarizes all reference potentials together used in this work with their free parameters p_Φ. The density distribution of these potentials is illustrated in Figure 1.

2.3. *Stellar Distribution Functions*

Throughout, we assume that the orbits of each MAP can be described by a single qDF of the form given by Binney & McMillan (2011). This is motivated by the findings of Bovy et al. (2012b,c,d) and Ting et al. (2013) about the simple phase-space structure of MAPs, and following Bovy & Rix (2013) and their successful application. This qDF has the form

$$\begin{aligned} &\mathrm{qDF}(\boldsymbol{J} \mid p_{\mathrm{DF}}) \\ &= f_{\sigma_R}(J_R, L_z \mid p_{\mathrm{DF}}) \times f_{\sigma_z}(J_z, L_z \mid p_{\mathrm{DF}}) \end{aligned} \qquad (2)$$

with

$$\begin{aligned} f_{\sigma_R}(J_R, L_z \mid p_{\mathrm{DF}}) &= n \times \frac{\Omega}{\pi \sigma_R^2(R_g) \kappa} \exp\left(-\frac{\kappa J_R}{\sigma_R^2(R_g)}\right) \\ &\quad \times [1 + \tanh(L_z/L_0)] \qquad (3) \\ f_{\sigma_z}(J_z, L_z \mid p_{\mathrm{DF}}) &= \frac{\nu}{2\pi\sigma_z^2(R_g)} \exp\left(-\frac{\nu J_z}{\sigma_z^2(R_g)}\right). \qquad (4) \end{aligned}$$

Here $R_g \equiv R_g(L_z)$ and $\Omega \equiv \Omega(L_z)$ are the (guiding-center) radius and the circular frequency of the circular orbit with angular momentum L_z in a given potential. $\kappa \equiv \kappa(L_z)$ and $\nu \equiv \nu(L_z)$ are the radial/epicycle (κ) and vertical (ν) frequencies with which the star would oscillate around the circular orbit in R- and z-direction when slightly perturbed (Binney & Tremaine 2008, §3.2.3) [TO DO: ask someone, if I'm messing up different definitions of κ]. The term $[1 + \tanh(L_z/L_0)]$ suppresses counter-rotation for orbits in the disk with $L \gg L_0$ which we set to a small value ($L_0 = 10 \times R_\odot/8 \times v_{\mathrm{circ}}(R_\odot)/220$ [TO DO: Jo said, galpy default is 10 km/s kpc. But I got the value actually from the code...]).

Table 1

Gravitational potentials of the reference galaxies used troughout this work and the respective ways to calculate actions in these potentials. All four potentials are axisymmetric. The potential parameters are fixed for the mock data creation at the values given in this table. In the subsequent analyses we aim to recover these potential parameters again. The parameters of `MW13-Pot` and `KKS-Pot` were chosen to resemble the `MW14-Pot` (see Figure 1). We use $v_{\rm circ}(R_\odot) = 230$ km s^{-1} for all potentials in this work.

name	potential type	potential parameters p_Φ		action calculation
`Iso-Pot`	isochrone potential[a] (Henon 1959)	b	0.9 kpc	***analytical and exact*** (Binney & Tremaine 2008, §3.5.2)
`KKS-Pot`	2-component Kuzmin-Kutuzov- Stäckel potential[b] (disk + halo) (Batsleer & Dejonghe 1994)	Δ $\left(\frac{a}{c}\right)_{\rm Disk}$ $\left(\frac{a}{c}\right)_{\rm Halo}$ k	0.3 20 1.07 0.28	***exact*** using *Stäckel Fudge* (Binney 2012) and interpolation on action grid[e] (Bovy 2015)
`MW13-Pot`	MW-like potential[c] with Hernquist bulge, spherical power-law halo, 2 exponential disks (stars + gas) (Bovy & Rix 2013)	R_d z_h f_h $\frac{{\rm d}\ln(v_{\rm circ}(R_\odot))}{{\rm d}\ln(R)}$	3 kpc 0.4 kpc 0.5 0	***approximate*** (same as `KKS-Pot`)
`MW14-Pot`	MW-like potential[d] with cut-off power-law bulge, Miyamoto-Nagai stellar disk, NFW halo (Bovy 2015)			***approximate*** (same as `KKS-Pot`)

[a] The isochrone potential `Iso-Pot` has one free parameter, the scale length b.

[b] The coordinate system of each of the two Stäckel-potential components of the `KKS-Pot` is $\frac{R^2}{\tau_{i,p}+\alpha_p} + \frac{z^2}{\tau_{i,p}+\gamma_p} = 1$ with $p \in \{\text{Disk}, /\text{Halo}\}$ and $\tau_{i,p} \in \{\lambda_p, \nu_p\}$. Both components have the same focal distance $\Delta \equiv \sqrt{\gamma_p - \alpha_p}$, to make sure that the superposition of the two components itself is still a Stäckel potential. The axis ratio of the coordinate surfaces $\left(\frac{a}{c}\right)_p := \sqrt{\frac{\alpha_p}{\gamma_p}}$ describes the flatness of the corresponding Stäckel component. The parameter k describes the relative contribution of the disk mass to the total mass.

[c] The free parameters of the `MW13-Pot` are stellar disk scale length R_d and height z_d, as well as the relative halo contribution to $v^2_{\rm circ}(R_\odot)$, f_h, and the slope of the rotation curve, $\frac{{\rm d}\ln(v_{\rm circ}(R_\odot))}{{\rm d}\ln(R)}$.

[d] The `MWPotential2014` by Bovy (2015) (see their Table 1) has a circular velocity at the Sun of $v_{\rm circ}(R_\odot) = 220$ km s^{-1}. In this work we use however $v_{\rm circ}(R_\odot) = 230$ km s^{-1} for all potentials.

[e] We use a finely spaced action interpolation grid with $R_{\rm max} = 10$ [TO DO: What's that??? units???] and 50 grid points in E and ψ [TO DO: Find out what's that???], and 60 grid points in L_z.

Table 2

Reference distribution-function parameters for the qDF in Equations (2)-(7). These qDFs describe the phase-space distribution of stellar MAPs for which mock data is created and analysed throughout this work for testing purposes. The parameters of the `cooler` & `colder` (`hotter` & `warmer`) MAPs were chosen to have the same $\sigma_{R,0}/\sigma_{z,0}$ ratio as the `hot` (`cool`) MAP. The `colder` and `warmer` MAPs have a free parameter X that governs how much colder/warmer they are then the reference `hot` and `cool` qDFs. Hotter populations have shorter tracer scale lengths (Bovy et al. 2012d) and the velocity dispersion scale lengths were fixed according to Bovy et al. (2012c).

name	qDF parameters $p_{\rm DF}$				
	h_R [kpc]	$\sigma_{R,0}$ [km s^{-1}]	$\sigma_{z,0}$ [km s^{-1}]	$h_{\sigma,R}$ [kpc]	$h_{\sigma,z}$ [kpc]
`hot`	2	55	66	8	7
`cool`	3.5	42	32	8	7
`cooler`	2 +50%	55-50%	66-50%	8	7
`hotter`	3.5-50%	42+50%	32+50%	8	7
`colder`	2 +X%	55-X%	66-X%	8	7
`warmer`	3.5-X%	42+X%	32+X%	8	7

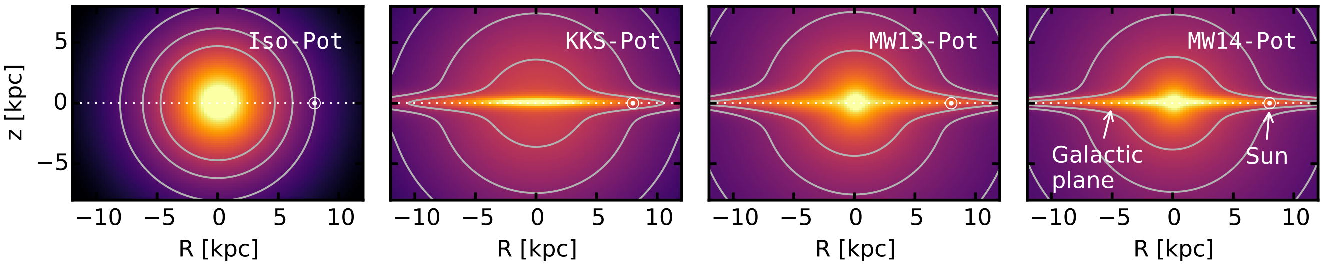

Figure 1. Density distribution of the four reference galaxy potentials in Table 1, for illustration purposes. These potentials are used throughout this work for mock data creation and potential recovery. [TO DO: Potential and/or population names in typewriter]

To match the observed properties of MAPs (see Bovy et al. 2012b,c,d), we chose the functional forms

$$n(R_g \mid p_{\mathrm{DF}}) \propto \exp\left(-\frac{R_g}{h_R}\right) \tag{5}$$

$$\sigma_R(R_g \mid p_{\mathrm{DF}}) = \sigma_{R,0} \times \exp\left(-\frac{R_g - R_\odot}{h_{\sigma,R}}\right) \tag{6}$$

$$\sigma_z(R_g \mid p_{\mathrm{DF}}) = \sigma_{z,0} \times \exp\left(-\frac{R_g - R_\odot}{h_{\sigma,z}}\right), \tag{7}$$

which indirectly set the stellar number density and radial and vertical velocity dispersion profiles. The qDF for each MAP has therefore a set of five free parameters p_{DF}: the density scale length of the tracers h_R, the radial and vertical velocity dispersion at the solar position $R_\odot$, $\sigma_{R,0}$ and $\sigma_{z,0}$, and the scale lengths $h_{\sigma,R}$ and $h_{\sigma,z}$, that describe the radial decrease of the velocity dispersion. Throughout this work we use for illustration purposes a few example stellar populations, each following a single qDF, whose parameters are given in in Table 2. Most tests use the `hot` and `cool` qDFs from Table 2, which correspond to kinematically hot and cool populations, respectively.

One crucial point in our dynamical modelling technique (§2.6), as well as in creating mock data (§2.5), is to calculate the (axisymmetric) spatial tracer density $\rho_{\mathrm{DF}}(\boldsymbol{x} \mid p_\Phi, p_{\mathrm{DF}})$ for a given qDF and potential . We do this by integrating the qDF at a given (R, z) over all three velocity components, using a N_v-th order Gauss-Legendre quadrature for each integral:

$$\begin{aligned}
&\rho_{\mathrm{DF}}(R, |z| \mid p_\Phi, p_{\mathrm{DF}}) \\
&= \int_{-\infty}^{\infty} \mathrm{qDF}(\boldsymbol{J}[R, z, \boldsymbol{v} \mid p_\Phi] \mid p_{\mathrm{DF}})\, \mathrm{d}^3\boldsymbol{v} &(8)\\
&\approx \int_{-n_\sigma \sigma_R(R|p_{\mathrm{DF}})}^{n_\sigma \sigma_R(R|p_{\mathrm{DF}})} \int_{-n_\sigma \sigma_z(R|p_{\mathrm{DF}})}^{n_\sigma \sigma_z(R|p_{\mathrm{DF}})} \int_0^{1.5 v_{\mathrm{circ}}(R_\odot)} \\
&\qquad \mathrm{qDF}(J[R, z, \boldsymbol{v} \mid p_\Phi] \mid p_{\mathrm{DF}})\, \mathrm{d}v_T\, \mathrm{d}v_z\, \mathrm{d}v_R, &(9)
\end{aligned}$$

where $\sigma_R(R \mid p_{\mathrm{DF}})$ and $\sigma_z(R \mid p_{\mathrm{DF}})$ are given by Equations 6 and 7 and the integration ranges are motivated by Figure 2. The integration range $[0, 1.5 v_{\mathrm{circ}}(R_\odot)]$ over v_T is in general sufficient (only for observation volumes at smaller Galactocentric radii with larger velocities this upper limit needs to be increased). For a given p_Φ and p_{DF} we explicitly calculate the density on $N_x \times N_x$ regular grid points in the (R, z) plane; in between grid points the density is evaluated with a bivariate spline interpolation. The grid is chosen to cover the extent of the observations (for $|z| \leq 0$, because the model is symmetric in z by construction). The total number of actions that need to be calculated to set up the density interpolation grid is $N_x^2 \cdot N_v^3$. §2.6 and Figure 3 show the importance of choosing N_x, N_v and n_σ sufficiently large in order to get the density with an acceptable numerical accuracy [TO DO: Jo thinks that this statement is difficult to understand here, because you have not yet talked about the normalization].

2.4. *Selection Functions*

Any survey's selection function can be understood as defining an effective sample subvolume in the space of observables: e.g. position on the plane of the sky (the survey area), distance from the sun (limited by the brightness of the stars and the sensitivity of the detector), colors and metallicity of the stars (limited by survey mode and targeting).
We simply use spatial selection functions, which describe the probability to observe a star at $\boldsymbol{x}$,

$$\mathrm{sf}(\boldsymbol{x}) \equiv \begin{cases} \mathrm{completeness}(\boldsymbol{x}) & \text{if } \boldsymbol{x} \text{ within observed volume} \\ 0 & \text{outside.} \end{cases}$$

For the observed volume we use simple geometrical shapes. Either a sphere of radius $r_{\max}$ with the sun at its center, or an angular segment of an cylindrical annulus (`wedge`), i.e. the volume with $R \in [R_{\min}, R_{\max}], \phi \in [\phi_{\min}, \phi_{\max}], z \in [z_{\min}, z_{\max}]$ within the model galaxy. The sharp outer cut of the survey volume could be understood as the detection limit in apparent brightness in the case, where all stars have the same luminosity. Here $0 \leq \mathrm{completeness}(\boldsymbol{x}) \leq 1$ everywhere inside the observed volume, so it can be understood as a position-dependent detection probability. Unless explicitly stated otherwise, we simplify to $\mathrm{completeness}(\boldsymbol{x}) = 1$.

2.5. *Mock Data*

We will rely on mock data as input to explore the limitations of the modelling. We investigate this, we assume first that our measured stars do indeed come from our assumed families of potentials and distribution functions and draw mock data from a given true distribution. Subsequently, we manipulate and modify these mock data sets to mimic observational effects.
The distribution function is given in terms of actions and angles. The transformation $(\boldsymbol{J}_i, \boldsymbol{\theta}_i) \longrightarrow (\boldsymbol{x}_i, \boldsymbol{v}_i)$ is however difficult to perform and computationally much more expensive than the transformation $(\boldsymbol{x}_i, \boldsymbol{v}_i) \longrightarrow (\boldsymbol{J}_i, \boldsymbol{\theta}_i)$. We employ a fast and simple two-step method for drawing mock data from an action distribution function, which also accounts effectively for a given survey selection function.

In the first step we draw positions $\boldsymbol{x}_i$ for our mock data stars from the selection function and tracer density. We start by setting up the interpolation grid for the tracer density $\rho(R, |z| \mid p_\Phi, p_{\mathrm{DF}})$ generated by the given qDF and according to §2.3 and Equation 9. For the creation of the mock data we use $N_x = 20$, $N_v = 40$ and $n_\sigma = 5$. Next, we sample random positions (R_i, z_i, ϕ_i) uniformly within the entire observable volume. Then we apply a rejection Monte Carlo method to these positions using the pre-calculated $\rho_{\mathrm{DF}}(R, |z| \mid p_\Phi, p_{\mathrm{DF}})$. To apply a non-uniform selection function, $\mathrm{sf}(\boldsymbol{x}) \neq$ const. within the observed volume, we use the rejection method a second time. The resulting sample then follows $\boldsymbol{x}_i \longrightarrow p(\boldsymbol{x}) \propto \rho_{\mathrm{DF}}(R, z \mid p_\Phi, p_{\mathrm{DF}}) \times \mathrm{sf}(\boldsymbol{x})$.

In the second step we draw velocities according to the distribution function. The velocities are independent of the selection function within the observed volume. For each of the positions (R_i, z_i) we sample velocities directly from the $\mathrm{qDF}(R_i, z_i, \boldsymbol{v} \mid p_\Phi, p_{\mathrm{DF}})$ using a rejection method. To reduce the number of rejected velocities, we use a Gaussian in velocity space as an envelope function, from which we first randomly sample velocities and

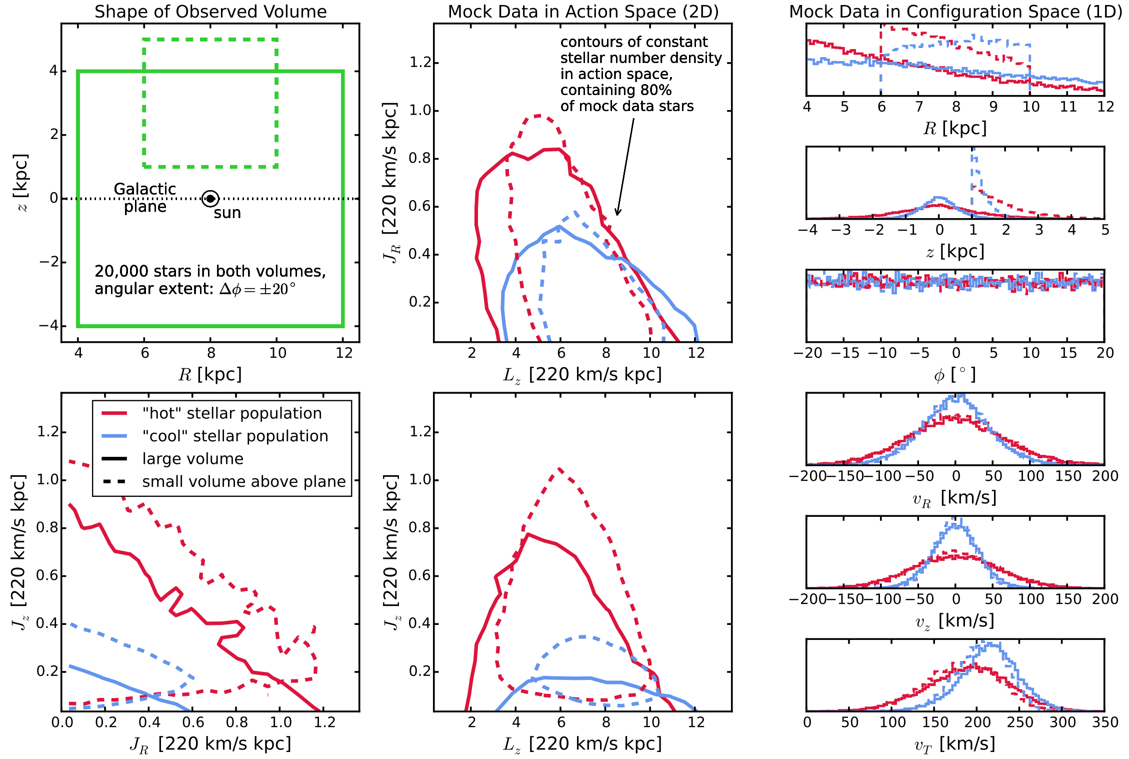

Figure 2. Distribution of mock data in action space (2D iso-density contours, enclosing 80% of the stars, the two central and the lower left panel) and configuration space (1D histograms, right panels), depending on shape and position of the survey observation volume and temperature of the stellar population. The parameters of the mock data model is given as Test 1 in Table 3. In the upper left panel we demonstrate the shape of the two different `wedge`-like observation volumes within which we were creating each a `hot` (red) and `cool` (blue) mock data set: a large volume centred on the Galactic plane (solid lines) and a smaller one above the plane (dashed lines). The distribution in action space visualizes how orbits with different actions also reach into different regions within the Galaxy. The 1D histograms on the right illustrate that qDFs generate realistic stellar distributions in galactocentric coordinates $(R, z, \phi, v_R, v_z, vT)$. [TO DO: fancybox Legend] [TO DO: Potential and/or population names in typewriter font] [TO DO: Jo suggests to make two or three separate figures out of this. I'm not yet convinced, as I think it is nice and tidy like this.]

then apply the rejection method to shape the Gaussian velocity distribution towards the velocity distribution predicted by the qDF. We now have a mock data satisfying $(\boldsymbol{x}_i, \boldsymbol{v}_i) \longrightarrow p(\boldsymbol{x}, \boldsymbol{v}) \propto \text{qDF}(\boldsymbol{x}, \boldsymbol{v} \mid p_\Phi, p_\text{DF}) \times \text{sf}(\boldsymbol{x})$.

Figure 2 shows examples of mock data sets in configuration space $(\boldsymbol{x}, \boldsymbol{v})$ and action space. The mock data from the qDF lead to the expected distributions in configuration space: More stars are found at smaller R and $|z|$, and are distributed uniformly in ϕ according to our assumption of axisymmetry. The distribution in radial and vertical velocities, v_R and v_z, is approximately Gaussian with the (total projected) velocity dispersion being $\sim \sigma_{R,0}$ and $\sim \sigma_{z,0}$ (see Table 2). The distribution of tangential velocities v_T is skewed because of asymmetric drift. The distribution in action space illustrates the intuitive physical meaning of actions: The stars of the `cool` population have in general lower radial and vertical actions, as they are on more circular orbits. The different relative distributions of the radial and vertical actions J_R and J_z of the `hot` and `cool` population is due to them having different velocity anisotropy $\sigma_{R,0}/\sigma_{z,0}$. The different ranges of angular momentum L_z in the two volumes reflect $L_z \sim Rv_\text{circ}$ and the different radial extent of both volumes. The volume above the plane contains stars with higher J_z, because stars with small J_z cannot reach that far above the plane. Circular orbits with $J_R = 0$ and $J_z = 0$ can only be observed in the Galactic mid-plane. An orbit with L_z much smaller or larger than $L_z(R_\odot)$ can only reach into a volume located around $R_\odot$, if it is more eccentric and has therefore larger J_R. This together with the effect of asymmetric drift can be seen in the asymmetric distribution of J_R in the top central panel of Figure 2.

If we want to add measurement errors to the mock data, we need to apply the following modifications to the above procedure. First, measurement errors are best described in heliocentric observables (see Section 2.1), we therefore assume and apply Gaussian errors to the *true* phase-space coordinates $\tilde{\boldsymbol{x}} = (\text{RA}, \text{DEC}, (m - M)), \tilde{\boldsymbol{v}} = (\mu_\text{RA}, \mu_\text{DEC}, v_\text{los})$, where we have taken $(m - M)$ as a proxy for distance. Second, in the case of distance errors, stars can virtually scatter in and out of the observed volume. To account for this, we draw the *true* positions from a volume that is larger than the actual observation volume, perturb the stars positions according to the distance errors and then reject all stars that lie now outside of the observed volume. This procedure mirrors the Poisson scatter around the detection threshold for stars whose distances are determined from the apparent brightness and the distance modulus. We then sample velocities (given the *true* positions of the stars) as described above and perturb them according to the measurement errors as well.

2.6. *Data Likelihood*

As data we consider here the positions and velocities of stars coming from a given MAP and survey selection function $\mathrm{sf}(\boldsymbol{x})$,

$$\begin{aligned}D = \{\boldsymbol{x}_i, \boldsymbol{v}_i \mid \quad &(\text{star } i \text{ belonging to same MAP})\\ &\wedge (\mathrm{sf}(\boldsymbol{x_i}) > 0)\}.\end{aligned}$$

The model that we fit is specified by a number of fixed and free parameters,

$$p_M = \{p_{\mathrm{DF}}, p_\Phi\}.$$

For the qDF parameters (see Section 2.3) we assume a prior that is flat in

$$p_{\mathrm{DF}} := \{\ln h_R, \ln \sigma_{R,0}, \ln \sigma_{z,0}, \ln h_{\sigma,R}, \ln h_{\sigma,z}\}. \quad (10)$$

The orbit of the i-th star in a potential with p_Φ is labeled by the actions $\boldsymbol{J}_i := \boldsymbol{J}[\boldsymbol{x}_i, \boldsymbol{v}_i \mid p_\Phi]$ and the qDF evaluated for the i-th star is then $\mathrm{qDF}(\boldsymbol{J}_i \mid p_M) := \mathrm{qDF}(\boldsymbol{J}[\boldsymbol{x}_i, \boldsymbol{v}_i \mid p_\Phi] \mid p_{\mathrm{DF}})$.

The likelihood of the data given the model is

$$\begin{aligned}&\mathscr{L}(D \mid p_M)\\ &\equiv \prod_i^N p(\boldsymbol{x}_i, \boldsymbol{v}_i \mid p_M)\\ &= \prod_i^N \frac{\mathrm{qDF}(\boldsymbol{J}_i \mid p_M) \cdot \mathrm{sf}(\boldsymbol{x}_i)}{\int \mathrm{d}^3x\, \mathrm{d}^3v\ \mathrm{qDF}(\boldsymbol{J} \mid p_M) \cdot \mathrm{sf}(\boldsymbol{x})}\\ &\propto \prod_i^N \frac{\mathrm{qDF}(\boldsymbol{J}_i \mid p_M)}{\int \mathrm{d}^3x\ \rho_{\mathrm{DF}}(R, |z| \mid p_M) \cdot \mathrm{sf}(\boldsymbol{x})}, \qquad (11)\end{aligned}$$

where N is the number of stars in the data set D, and in the last step we used Equation 9. The factor $\prod_i \mathrm{sf}(\boldsymbol{x}_i)$ is independent of the model parameters so we treat it as unimportant proportionality factor in the likelihood calculation. We find the best set of model parameters by maximizing the posterior probability distribution $pdf(p_M \mid D)$, which is according to Bayes' theorem proportional the likelihood $\mathscr{L}(D \mid p_M)$ times the prior. We assume flat priors in both p_Φ and p_{DF} (see Equation 10) through out this work, then *pdf* and likelihood can and will be used interchangeably for the remainder of the work.

The normalisation in Equation 11 is a measure for the total number of tracers inside the survey volume,

$$M_{\mathrm{tot}} \equiv \int \mathrm{d}^3x\ \rho_{\mathrm{DF}}(R, |z| \mid p_M) \cdot \mathrm{sf}(\boldsymbol{x}). \qquad (12)$$

In the case of an axisymmetric galaxy model and $\mathrm{sf}(\boldsymbol{x}) = 1$ everywhere inside the observed volume (i.e. a complete sample as assumed in most tests in this work), the normalisation is essentially a two-dimensional integral in R and z of the interpolated tracer density ρ_{DF} in Equation 9 over the differential survey volume, i.e. $\frac{\partial M_{\mathrm{tot}}}{\partial \phi}(R, z) = \int \mathrm{d}R\ \mathrm{d}z\ \rho_{\mathrm{DF}} \times \frac{\partial V}{\partial \phi}$ [TO DO: missing factor of R???]. We perform this integral as a Gauss Legendre quadrature of order 40 in each R and z direction. The angular integral, i.e. $M_{\mathrm{tot}} = \int R\, \mathrm{d}\phi\ \frac{\partial M_{\mathrm{tot}}}{\partial \phi}$, can be solved analytically.

It turns out that the sufficiently accurate evaluation of the likelihood is computationally expensive, even for only one set of model parameters. This expense is dominated by the number of action calculations required, which in turn depends on the number of stars in the sample and the numerical accuracy of the integrals in Equation 9 needed for the normalisation, which requires $N_x^2 \times N_v^3$ action calculations. The accuracy has to be chosen high enough, such that a resulting numerical error

$$\delta_{M_{tot}} \equiv \frac{M_{\mathrm{tot,approx}}(N_x, N_v, N_\sigma) - M_{\mathrm{tot}}}{M_{\mathrm{tot}}} \qquad (13)$$

[TO DO: make sure every Mtottrue is replaced by Mtot] does not dominate the likelihood, i.e.

$$\begin{aligned}&\log \mathscr{L}(p_M \mid D)\\ &= \sum_i^N \log \mathrm{qDF}(\boldsymbol{J_i} \mid p_M) - 3N \log (r_o v_o)\\ &-N \log(M_{\mathrm{tot}}) - N \log(1 + \delta_{M_{tot}}), \qquad (14)\end{aligned}$$

with

$$N \log(1 + \delta_{M_{tot}}) \lesssim 1.$$

In other words, this error is only small enough if it does not affect the comparison of two adjacent models whose log-likelihoods differ, to be clearly distinguishable, by 1. Otherwise numerical inaccuracies could lead to systematic biases in the potential and DF fitting. For data sets as large as $N = 20{,}000$ stars, which in the age of Gaia could very well be the case [TO DO: Really???], one needs a numerical accuracy of 0.005% in the normalisation. Figure 3 demonstrates that the numerical accuracy we use in the analysis, $N_x = 16$, $N_v = 24$ and $N_{sigma} = 5$, does satisfy this requirement.

[TO DO: Comment by HW: What I am missing in this Section is any distinction of what aspects are ”new” (not addressed in existing papers) and what is recapitulated to be coherent.]

If the data is affected by measurement errors, they have to be incorporated in the likelihood. We assume Gaussian errors in the observable space $\boldsymbol{y} \equiv (\tilde{\boldsymbol{x}}, \tilde{\boldsymbol{v}}) = (\mathrm{RA}, \mathrm{DEC}, (m - M), \mu_{\mathrm{RA}}, \mu_{\mathrm{DEC}}, v_{\mathrm{los}})$, i.e. the i-th star's observed $\boldsymbol{y}_i \sim N[\boldsymbol{y'}_i, \delta\boldsymbol{y}_i](\boldsymbol{y}) = N[\boldsymbol{y}, \delta\boldsymbol{y}_i](\boldsymbol{y'}_i)$ [TO DO: Talk to HW about best notation.], with $\boldsymbol{y}_i{}'$ being the true position and velocity of the star. Stars follow the (quasi-isothermal) distribution function ($\mathrm{DF}(\boldsymbol{y'}) \equiv \mathrm{qDF}(\boldsymbol{J}[\boldsymbol{y'} \mid p_\Phi] \mid p_{\mathrm{DF}})$ for short), convolved with the error distribution $N[0, \delta\boldsymbol{y}](\boldsymbol{y'})$ [TO DO: CHECK AGAIN]. The selection function $\mathrm{sf}(\boldsymbol{y})$ acts on the space of (error affected) observables. Then the probability of one star becomes

$$\begin{aligned}&\tilde{p}(\boldsymbol{y}_i \mid p_\Phi, p_{\mathrm{DF}}, \delta\boldsymbol{y}_i)\\ &\equiv \frac{\mathrm{sf}(\boldsymbol{y}_i) \cdot \int \mathrm{d}^6y'\ \mathrm{DF}(\boldsymbol{y'}) \cdot N[\boldsymbol{y}_i, \delta\boldsymbol{y}_i](\boldsymbol{y'})}{\int \mathrm{d}^6y'\ \mathrm{DF}(\boldsymbol{y'}) \cdot \int \mathrm{d}^6y\ \mathrm{sf}(\boldsymbol{y}) \cdot N[\boldsymbol{y'}, \delta\boldsymbol{y}_i](\boldsymbol{y})}.\end{aligned}$$

In the case of errors in distance or position, the evaluation of this is computational expensive - especially if the stars have heteroscedastic errors $\delta\boldsymbol{y}_i$, for which the normalisation would have to be calculated for each star

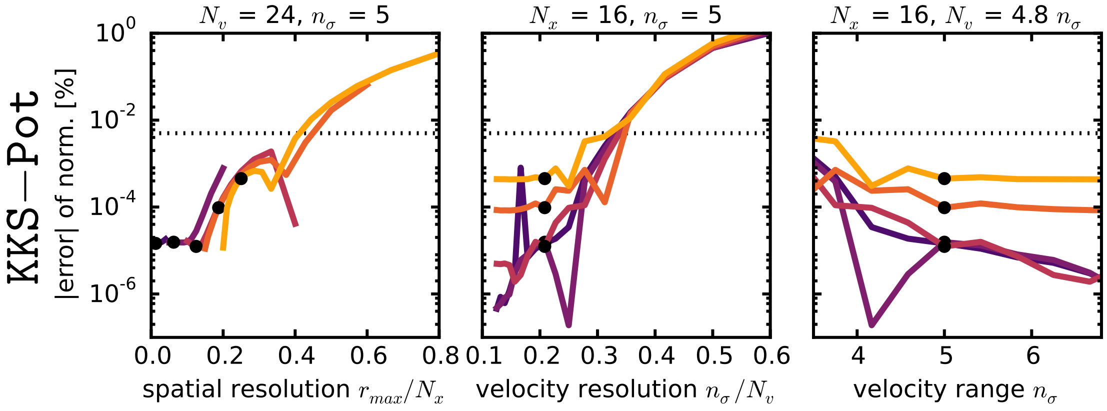

Figure 3. Relative error $\delta M_{\rm tot}$ of the likelihood normalization $M_{\rm tot}$ in Equation 13 depending on the accuracy of the grid-based density calculation in Equation 9 (and surrounding text). We show how $\delta M_{\rm tot}$ varies with the spatial resolution (first column), velocity resolution (second column) and velocity integration range (third column) for two different potentials (`KKS-Pot` in the first row and `MW13-Pot` in the second row) and five different spherical observation volumes with radius $r_{\rm max}$ (color coded according to the legend). (Test 2 in Table 3 summarizes all model parameters.) N_x is the number of spatial grid points in $R \in R_\odot {\rm kpc} \pm r_{\rm max}$ and $|z| \in [0, r_{\rm max}]$ on which the density is evaluated according to Equation 9. The spatial resolution in z is therefore $r_{\rm max}/N_x$ and $2r_{\rm rmax}/N_x$ in R. This choice is reasonable because the density is symmetric in z and varies less in R than in z, because the tracer scale length of the disk is much larger than its scale height. At each (R, z) of the grid a Gauss-Legendre integration of order N_v is performed over an integration range of $\pm n_\sigma$ times the velocity dispersion in v_R and v_z and $[0, 1.5 v_{\rm circ}(R_\odot)]$ in v_T. n_σ/N_v is therefore a proxy for the velocity resolution of the grid. (We vary N_x, N_v and n_σ separately and keep the other two fixed at the values indicated above the columns.) To arrive at the approximation $M_{\rm tot,approx}$ for $M_{\rm tot}$ in Equation 12, we perform a 40th-order Gauss-Legendre integration in each R and z direction of the interpolated density over the observed volume. We calculate the "true" normalization with high accuracy as $M_{\rm tot} \approx M_{\rm tot,approx}(N_x = 20, N_v = 56, N_\sigma = 7)$. The black dots indicate the accuracy used in our analyses: It is better than 0.002%. Only for the smallest volume in the `MW13-Pot` (yellow line) the error is only $\sim 0.005\%$. This could be due to the fact, that, while we have analytical formulas to calculate the actions for the Staeckel potential `KKS-Pot` exactly, we have to resort to an approximate action calculation for the MW-like potential `MW13-Pot` (see Section 2.2). [TO DO: Write $|\delta M_{\rm tot}|$ on y-axis] [TO DO: Remove MW13-Pot completely from this plot, caption and test table] [TO DO: Caption too long] [TO DO: Rewrite caption, text and table, I changed the plot]

separately. In practice we apply the following approximation,

$$\tilde{p}(\boldsymbol{y}_i \mid p_\Phi, p_{\rm DF}, \delta\boldsymbol{y}_i)$$
$$\approx \frac{{\rm sf}(\boldsymbol{x}_i)}{\int {\rm d}^6y' \; {\rm DF}(\boldsymbol{y}') \cdot {\rm sf}(\boldsymbol{x}')} \cdot \frac{1}{N_{\rm error}} \sum_n^{N_{\rm error}} {\rm DF}(\boldsymbol{x}_i, \boldsymbol{v}[\boldsymbol{y}'_{i,n}]) \tag{15}$$

with

$$\boldsymbol{y}'_{i,n} \sim N[\boldsymbol{y}_i, \delta\boldsymbol{y}_i](\boldsymbol{y}')$$

In doing so, we ignore errors in the star's position $\boldsymbol{x}_i$ [TO DO: something is not clear to HW here] altogether. This simplifies the normalisation drastically and makes it independent of measurement errors, including the velocity errors. Distance errors however are included [TO DO: something is not clear to HW here], but only implicitly in the convolution over the stars' velocity errors in the Galactocentric rest frame. We calculate the convolution using Monte Carlo integration with $N_{\rm error}$ samples drawn from the full error Gaussian in observable space, $y'_{i,n}$.

2.7. *Fitting Procedure*

To search the $(p_\Phi, p_{\rm DF})$ parameter space for the maximum of the likelihood in Equation 11, we go beyond the fixed grid search by Bovy & Rix (2013) and employ an effective two-step procedure: The first step finds the approximate peak and width of the likelihood using a nested-grid search, while the second step samples the shape of the likelihood using a Monte-Carlo Markov Chain (MCMC) approach.

Fitting Step 1: Nested-grid search.— The $(p_\Phi, p_{\rm DF})$ parameter space can be high-dimensional. To effectively minimizing the number of likelihood evaluations before finding its peak, we use a nested-grid approach:

- *Initialization.* For N free model parameters $M = (p_\Phi, p_{\rm DF})$, we set up a sufficiently large initial grid with 3^N regular grid points.
- *Evaluation.* We evaluate the likelihood at each grid-point similar to Bovy & Rix (2013) (their Figure 9): Because of the many computationally expensive $\boldsymbol{x}, \boldsymbol{v} \xrightarrow{p_\Phi} \boldsymbol{J}$ transformations that have to be performed for each new set of p_Φ parameters, an outer loop iterates over the p_Φ parameters and pre-calculates the actions, while an inner loop evaluates the likelihood Equation 11 for all qDF parameters $p_{\rm DF}$ with the actions in the given potential.
- *Iteration.* To find from the very sparse 3^N likelihood grid a new grid, that is more centered on the likelihood and has a width of order of the width of the likelihood, we proceed as follows: For each of the model parameter in M we marginalize the likelihood by summing over the grid. If the resulting 3 points all lie within 4σ of a Gaussian, we fit a Gaussian to the 3 points and determine a new 4σ fitting range. Otherwise the boundaries of the grid point with the highest likelihood becomes the new fitting range. We proceed with iteratively evaluating the likelihood on finer and finer grids, until we have found a 4-sigma fit range in each of the model parameter dimensions.
- *The fiducial qDF.* For the above strategy to work

properly, the action pre-calculations have to be independent of the choice of qDF parameters. This is clearly the case for the $N_j \times N_{\rm error}$ stellar data actions $\boldsymbol{J}_i$. To calculate the normalisation in Equation 11, $N_x^2 \times N_v^3$ actions $\boldsymbol{J}_n$ are needed. Formally the spatial coordinates at which the $\boldsymbol{J}_n$ are calculated depend on the $p_{\rm DF}$ parameters via the integration ranges in Equation 9. To relax this dependence we instead use the same velocity integration limits in the likelihood calculations for all $p_{\rm DF}$s in a given potential. This set of parameters, that sets the velocity integration range globally, $(\sigma_{R,0}, \sigma_{z,0}, h_{\sigma,R}, h_{\sigma,z})$ in Equation 6 and 7, is referred to as the *fiducial* qDF. Using the same integration range in the density calculation for all qDFs at a given p_Φ makes the normalisation vary smoothly with different $p_{\rm DF}$. Choosing a fiducial qDF that is very different from the true qDF can however lead to large biases. The optimal values for the fiducial qDF are the (yet unknown) best fit $p_{\rm DF}$ parameters. We take care of this by setting, in each iteration step of the nested-grid search, the fiducial qDF simply to the $p_{\rm DF}$ parameters of the central grid point. As the nested-grid search approaches the best fit values, the fiducial qDF approaches automatically the optimal values as well. This is another advantage of the nested-grid search, because the result will not be biased by a poor choice of the fiducial qDF.

- *Computational expense.* Overall the computation speed of this nested-grid approach is dominated (in descending order of importance) by a) the complexity of potential and action calculation, b) the number $N_j \times N_{\rm error} + N_x^2 \times N_v^3$ of actions to calculate, i.e. the number of stars, error samples and numerical accuracy of the normalisation calculations, c) the number of different potentials to investigate (i.e. the number of free potential parameters and number of grid points in each dimension) and d) the number of qDFs to investigate. The latter is also non-negligible, because for such a large number of actions the number of qDF-function evaluations also take some time.

Fitting Step 2: MCMC.— After the nested-grid search is converged, the grid is centered at the peak of the likelihood and its extent contains the 4σ confidence interval. To actually sample the full shape of the likelihood, we could do a grid search with much finer grid spacing (e.g. $K = 11$ in each dimension). The number of grid points scales as a power of the free parameters N. For a large number of free parameters ($N > 4$) a Monte Carlo Markov Chain (MCMC) approach might sample the *pdf* (which is here equivalent to the likelihood, see §2.6) much faster. We use *emcee* by Foreman-Mackey et al. (2013) and release the walkers very close to the *pdf* peak found by the nested-grid search, which will assure fast convergence in much less than K^N likelihood evaluations.
For a sufficiently high numerical accuracy in calculating the integrals in Equation 9 the current qDF at each walker position can be used as the fiducial qDF. To get reasonable results also for slightly lower accuracy, a single fiducial qDF can be used for all likelihood evaluations within the MCMC as well. As fiducial qDF we use the qDF parameters of the likelihood peak, found by the nested-grid search.

[TO DO: Make consistent use of *pdf* and likelihood.]

3. RESULTS

We are now in a position to explore the limitations of action based modelling posed in the introduction: (i) unbiased estimates; (ii) survey volume; (iii) imperfect selection function; (iv) measurement errors; (v) actual DF or (vi) Potential not spanned by the space of models. We do not explore the breakdown of the assumption that the system is axisymmetric and in steady state. With the exception of the test suite on measurement errors in §3.4, we assume that the phase-space errors are negligible. All tests are also summarized in Table 3.

[TO DO: Hans-Walter said that there are diagnostic plots in this papers that can be eliminated and their essence summarized in 1-2 sentences in the text. Fine. But which plots does he think can be eliminated? My plots contain either results or are only there to make the paper more readable for others.]

3.1. *Model Parameter Estimates in the Limit of Large Data Sets*

The individual MAPs in Bovy & Rix (2013) contained typically between 100 and 800 objects, so that each MAP implied a quite broad *pdf* for the model parameters $p_M = \{p_\Phi, p_{\rm DF}\}$. Here we explore what happens in the limit of much larger samples for each MAP, say 20,000 objects. As outlined in §2.6 the immediate consequence of larger samples is given by the likelihood normalization requirement, $\log(1 + \delta M_{\rm tot}) \leq 1/N_{sample}$, (see Equation 14)), which is the modelling aspect that drives the computing time. This issues aside, we would, however, expect that in the limit of large data sets with vanishing measurement errors the *pdf*s of the p_M become Gaussian, with a *pdf* width (i.e. standard error SE of the Gaussian) that scales as $1/\sqrt{N_{\rm sample}}$. Further, we must verify that any bias in the *pdf* expectation value is considerably less than the error (SE), even for quite large samples.

Using sets of mock data, created according to §2.5 and the fiducial model for p_M (see Table 3, Tests 3.2, 3.3, and 3.1), we verified that *RoadMapping* satisfies all these conditions and expectations. Figure 4 illustrates the joint *pdf*s of all p_M. This figure illustrates that the *pdf* is a multivariate Gaussian that projects into Gaussians when considering the marginalized *pdf* for all the individual p_M. Note that some of the parameters are quite covariant, but the level of their actual covariance depends on the choice of the p_M from which the mock data were drawn. Figure 5 then illustrates that the *pdf* width, SE, indeed scales as $1/\sqrt{N_{\rm sample}}$. Figure 6 illustrates even more that *RoadMapping* satisfies the central limit theorem. The average parameter estimates from many mock samples with identical underlying p_M are very close to the input p_M, and the distribution of the actual parameter estimates are a Gaussian around it.

[TO DO: I sometimes talk about pdf, sometimes about likelihood. We should make this consistent everywhere. I would use *pdf* everywhere, but I sometimes reference the likelihood equation. How should I write it in this case?]

3.2. *The Role of the Survey Volume Geometry*

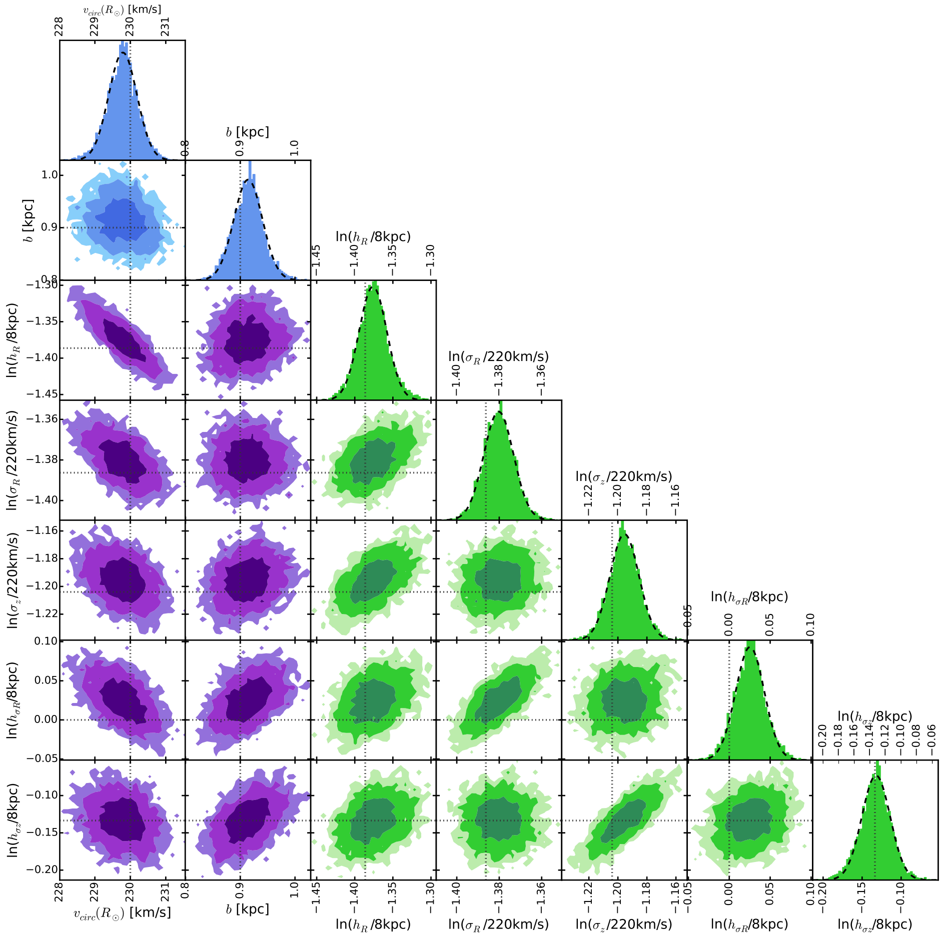

Figure 4. The *pdf* (proportional to the likelihood in Equation [TO DO]) in the parameter space $p_M = \{p_\Phi, p_{\rm DF}\}$ for one example mock data set created according to Test 3.1 in Table 3. Blue indicates the *pdf* for the potential parameters, green the qDF parameters. The true parameters are marked by dotted lines. The dark, medium and bright contours in the 2D distributions represent 1, 2 and 3 sigma confidence regions [TO DO: HW: "likelihood vs. pdf - This is where this matters: is this a confidence on the data or on the parameters?" Don't understand, what he means...], respectively, and show weak or moderate covariances. This analysis was picked among five similar analyses, to have all 1 sigma contours encompass the input values [TO DO: Jo didn't understand this sentence]. The *pdf* here was sampled using MCMC (with flat priors in p_Φ and $\ln(p_{\rm DF})$ to turn the likelihood in Equation 11 into a full *pdf*). Because only 10,000 MCMC samples were used to create the histograms shown, the 2D distribution has noisy contours. The dashed lines in the 1D distributions are Gaussian fits to the histogram of MCMC samples. This demonstrates very well that for such a large number of stars, the *pdf* approaches the shape of a multi-variate Gaussian, as expected from the central limit theorem [TO DO: Jo wrote, that he is not sure if the central limit theorem is directly relevant here]. [TO DO: rename $h_{\sigma R}$ to $h_{\sigma,R}$, σ_R to $\sigma_{R,0}$ and analogous for z]

To explore the role of the survey volume (see Section 1) at given sample size, we devise two suites of mock data sets:

The first suite draws mock data from the same p_M, *two different potentials* (`Iso-Pot` and `MW13-Pot`, see Test 4 in Table 3), and volume wedges (see Section 2.4) at *different positions within the Galaxy*, illustrated in the right upper panel of Figure 7. To isolate the role of the survey volume geometry, the mock data sets are equally large (20,000) in all cases, and are drawn from identical total survey volumes (4.5 kpc^3, achieved by adjusting the angular width of the wedges). The results are shown in Figure 7.

The second suite of mock data sets was already introduced in Section 3.1 (see also Test 3.3), where mock data sets were drawn from five spherical volumes around the sun with different maximum radius, for *two different stellar populations*. The results of this second suite are shown in Figure 6 and demonstrate the effect of the *size of the survey volume*.

Figures 6 and 7 illustrate the ability of *RoadMapping* to constrain model parameters, with the standard error of the *pdf* as measure of the precision on the x-axis. Figure 6 demonstrates that, given a choice of qDF, a larger volume always results in tighter constraints. There is no obvious trend that a hotter or cooler MAP will always give better results [TO DO: Comment from HW: The question of whether a hotter or a colder population gives tighter constraints is an important question, but it seems buries here in a section that is dedicated to another matter, namely the question of volume ... It's OK to leave it here, but somewhere we need to say clearly: whether the population is hot or cold does not make a big and generic difference...]; it depends on the survey volume and the model parameter in question. In Figure 7 the wedges all have the same volume and all give results of similar precision. Minor differences, e.g. with the `Iso-Pot` potential being less constrained in the wedge with large vertical, but small radial extent, are a special property of the considered potential and parameters, and not a

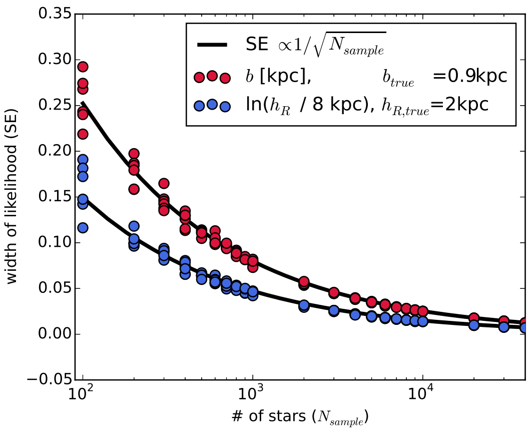

Figure 5. The width of the *pdf* for two fit parameters found from analyses of 132 mock data sets vs. the number of stars in each data set. The mock data was created in the Iso-Pot potential and all model parameters are given as Test 3.2 in Table 3. The *pdf* (using the likelihood in Equation 11 [TO DO: CHECK]) was evaluated and then a Gaussian was fitted to the marginalized *pdf* of each free fit parameter. The standard error (SE) of these best fit Gaussians is shown for the potential parameter b in kpc (red dots) and for the qDF parameter $\ln(h_R/8\text{kpc})$ in dimensionless units (blue). The black lines are fits of the functional form $\text{SE}(N_\text{sample}) \propto 1/\sqrt{N_\text{sample}}$ to the data points of both shown parameters. As can be seen, for large data samples the width of the *pdf* behaves as expected and scales with $1/\sqrt{N_\text{sample}}$ as predicted by the central limit theorem. [TO DO: fancybox Legend] [TO DO: write pdf instead of likelihood on y-axis] [TO DO: axis labels similar to MC_vs_error plot.] [TO DO: Different colors (blue and green), and different markers (no black rings).]

global property of the corresponding survey volume. In the case of an axisymmetric model galaxy, the extent in ϕ direction is not expected to matter. Overall radial extent and vertical extent seem therefore to be equally important to constrain the potential. In addition Figure 7 implies that for these cases volumes offsets in the radial or vertical direction have at most a modest impact - even in case of the very large sample size at hand.
While it appears that the argument for significant radial and vertical extent is generic, we have not done a full exploration of all combinations of p_M and volumina.

3.3. *Impact of Misjudging the Completeness of the Data Set*

The completeness function (see Section2.4) depends on the characteristics and mode of the survey. It can be very complex and is therefore sometimes not perfectly known. We investigate how much the recovery of the potential can be affected by imperfect knowledge of the selection function. We do this by creating mock data with varying incompleteness (within a maximal survey volume), while assuming constant completeness in the analysis. The mock data comes from a sphere around the sun with an incompleteness function that drops linearly with distance r from the sun (see Test 5, Example 1, in Table 3 and Figure 8). This captures the relevant case of stars being less likely to be observed (than assumed) the further away they are (e.g. due to unknown dust obscuration). We demonstrate that the potential recovery with *RoadMapping* is very robust against somewhat wrong assumptions about the radial completeness of the data (see Figure 9). Apparently, much information about the potential comes from the rotation curve measurements in the plane, which is not affected by the incompleteness of the sample. In Appendix .1 we also show that the robustness is somewhat less striking but still persists for small misjudgments of the incompleteness in vertical direction, parallel to the disk plane (Figures 20 and 21). This could model the effect of wrong corrections for interstellar extinction in the plane. We also investigate in Appendix .1 if indeed most of the information is stored in the rotation curve [TO DO: Comment by HW: I don't have an immediate solution for this, but again, it seems the interesting question of "how much of the information is in the rotation curve" is 'hidden' in the section on selection functions...]. For this we use the same mock data sets as analysed in Figures 9 and 21, but without including the tangential velocities in the modelling (by marginalizing the likelihood over v_T). In this case the potential is much less tightly constrained, even for 20,000 stars. For only small deviations of true and assumed completeness ($\lesssim 10\%$) we can however still incorporate the true potential in our fitting result (see Figure 22).

[TO DO: Mention in text or caption how the panels looked that I removed.]

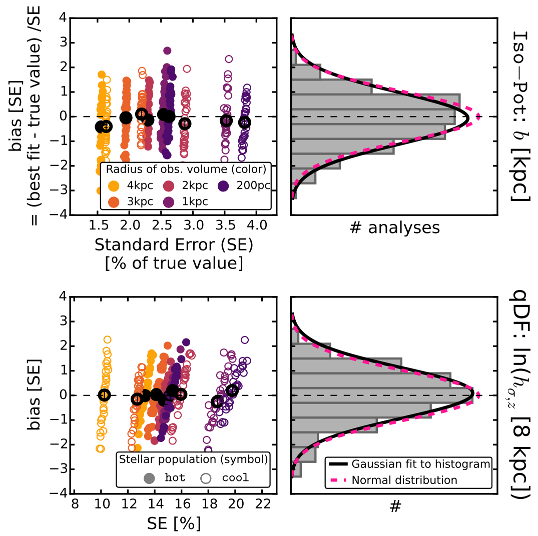

Figure 6. (Un-)bias of the parameter estimates: According to the central limit theorem the the best fit values for a large number of data sets, each containing a large number of stars, will follow the Normal distribution. To test this, we create 320 mock data sets, which come from two different stellar populations and five spherical observation volumes (see legends). All model parameters are summarized in Table 3 as Test 3.3. Bias and relative standard error (SE) are derived from the marginalized *pdf* for one potential parameter (isochrone scale length b in first row) and one qDF parameter ($h_{\sigma,z}$ in second row). The second column displays a histogram of the 320 offsets. As it closely follows a Normal distribution, our modelling method is therefore well-behaved and unbiased. For the 32 analyses belonging to one model we also determine the mean offset and SE, which are overplotted in black in the first two columns (with $1/\sqrt{32}$ as error). [TO DO: Is the scatter of the black symbols too large??? Is the reason for this numerical inaccuracies???] [TO DO: Change test table accordingly, isochrone with b = 1.5 is not used anymore] [TO DO: Caption is too long. Make shorter.] [TO DO: r_max instead of radius in legend] [TO DO: Leerzeichen fehlt in y-achsenbeschriftung]

3.4. *Measurement Errors and their Effect on the Parameter Recovery*

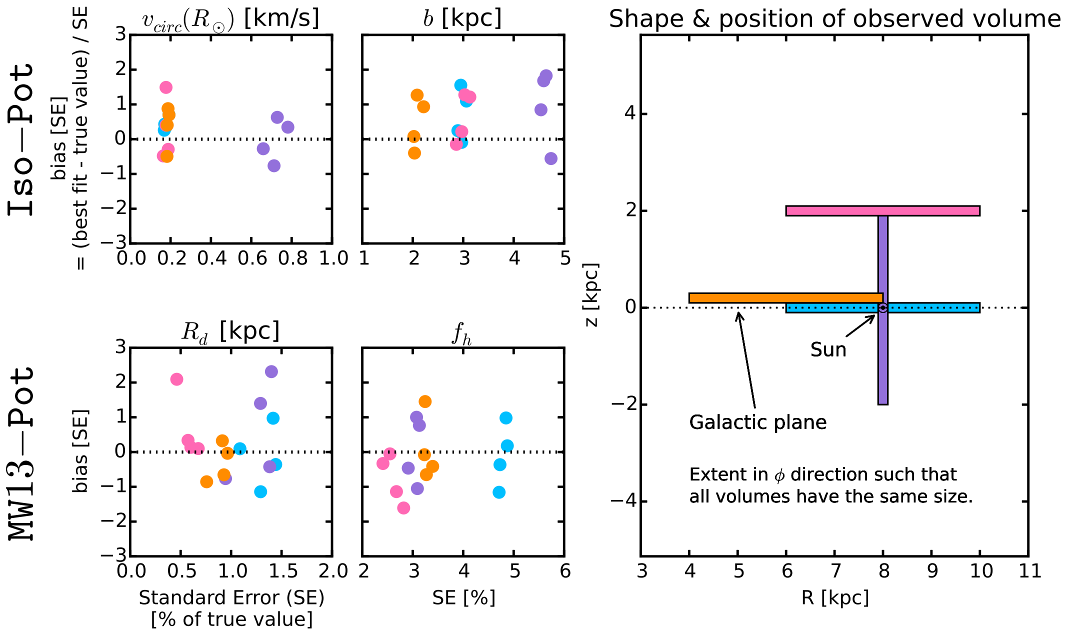

Figure 7. Bias vs. standard error in recovering the potential parameters for mock data stars drawn from four different test observation volumes within the Galaxy (illustrated in the upper right panel) and two different potentials (`Iso-Pot` and `MW13-Pot` from Table 1). Standard error and offset were determined as in Figure 6. Per volume and potential we analyse four different mock data realisations; all model parameters are givenas Test 4 in Table 3. The colour-coding represents the different wedge-shaped observation volumes. The angular extent of each wedge-shaped observation volume was adapted such that all have the volume of 4.5 kpc^3, even though their extent in (R, z) is different. Overall there is no clear trend, that an observation volume around the sun, above the disk or at smaller Galactocentric radii should give remarkably better constraints on the potential than the other volumes. [TO DO: Write in Plot "... that all wedges have the same volume".

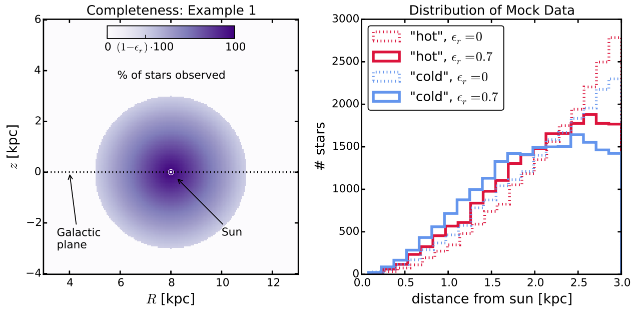

Figure 8. Selection function and mock data distribution for investigating radial incompleteness of the data. All model parameters are summarized as Test 5, Example 1, in Table 3. The survey volume is a sphere around the sun and the percentage of observed stars is decreasing linearly with radius from the sun, as demonstrated in the left panel. How fast this detection/incompleteness rate drops is quantified by the factor ϵ_r. Histograms for four data sets, drawn from two MAPs (`hot` in red and `cool` in blue, see Table 2) and with two different ϵ_r, 0 and 0.7, are shown in the right panel for illustration purposes. [TO DO: Potential and/or population names in typewriter font]

[TO DO: Comment from HW: This Section has three parts:
– convergence of the integral
– testing the approximation
– underestimating errors
It seems to me that the basic Section: What is the impact of the errors? Is missing. That should be the center piece, and the other three aspects should be quick summary notes, only 1-2 sentences long.] [I'll try to address this with a plot mean(SE) vs. proper motion error - also for cold population (currently running on wolf).]

Convergence of the error integral. — [TO DO: Move this section and plot to theory part.] In Section 2.6 we introduced how we convolve the model probability with the measurement errors. In the absence of distance errors, the accuracy of the parameter recovery is limited by insufficient sampling of the MC convolution integral in Equation 15. Test 6.1 in Table 3 and Figure 10 investigate how many MC samples are needed, given the size of the velocity error, for the integral to be accurate within certain limits: For each $\delta\mu \in [2, 3, 4, 5]$ mas yr^{-1} we set up $N_{\text{mock}} = 4$ mock data sets and evaluate the likelihood for different N_{error}. We used $N_{\text{conv}} = 800$ and 1200 MC samples to calculate the numerically converged likelihood for proper motion errors $\delta\mu \leq 3$mas yr^{-1} and $\delta\mu > 3$mas yr^{-1}, respectively (see left panels in Figure 11). We determined the bias

$$\text{BIAS}(N_{\text{error}}, \delta\mu) \equiv \frac{1}{N_{\text{mock}}} \sum_{j=1}^{N_{\text{mock}}} \left[\langle p_i \rangle (N_{\text{error}}, \delta\mu)\right]_j - \left[\langle p_i \rangle (N_{\text{conv}}, \delta$$

where $[\langle p_i \rangle (N_{\text{error}}, \delta\mu)]_j$ is the best estimate for the i-th model parameter $p_i \in p_M$ from the analysis of the j-th mock data realisation with $\delta\mu$ using N_{error} MC samples. From this we then generated the curves $N_{\text{error},i}(\delta v_{\text{max}}, \text{BIAS})$ in Figure 10 by linear interpolation, that show how many MC samples are needed for parameter p_i given a velocity error and a systematic bias in units of the standard error (SE) of the estimate. The proper motion error $\delta\mu$ translates to heteroscedastic [TO DO: make sure that this word is written correctly every-

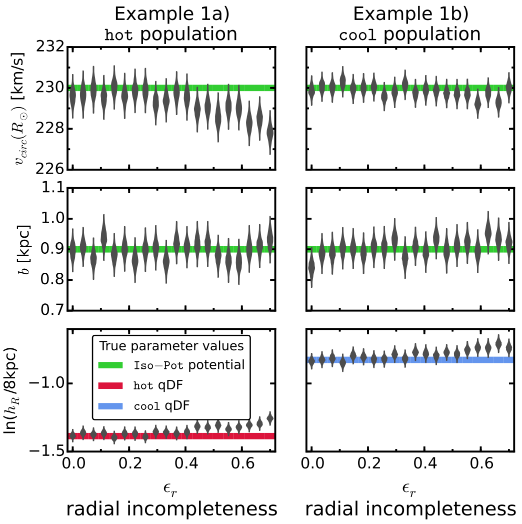

Figure 9. Influence of wrong assumptions about the radial incompleteness of the data on the parameter recovery with *RoadMapping*. Each mock data set was created with different incompleteness parameters ϵ_r (shown on the x-axis and illustrated in Figure 8) and the model parameters are given as Test 5, Example 1, in Table 3. The analysis however did not know about the incompleteness and assumed that all data sets had constant completeness within the survey volume ($\epsilon_r = 0$). The marginalized likelihoods from the fits are shown as violins. The green lines mark the true potential parameters (Iso-Pot) and the red and blue lines the true qDF parameters (hot MAPin red and cool MAPin blue), which we tried to recover. The *RoadMapping* method seems to be very robust against small to intermediate deviations between the true and the assumed data incompleteness. [TO DO: Jo suggested to also remove the h_R panel, but I like, that one can see that it is the spatial tracer distribution that drives the little degradation of the recovery.]

where.] velocity errors according to

$$\delta v[\mathrm{km\ s}^{-1}] \equiv 4.74047 \cdot r[\mathrm{kpc}] \cdot \delta\mu[\mathrm{mas\ yr}^{-1}], \qquad (16)$$

where r is the distance of the star to the sun. The largest velocity error $\delta v_{\max}$ within the sample is at $r_{\max}$. We find in Figure 10 the relation

$$N_{\mathrm{error},i}(\delta v_{\max}, \mathrm{BIAS}) \propto (\delta v_{\max})^2 .$$

Figure 10 also demonstrates that different model parameters do not have the same sensitivity to the numerical inaccuracies introduced by insufficient sampling. [TO DO: Comment from Jo: I think it is important to test, if the MC vs error plot depends on number pf stars. Maybe test it with less stars (5000), to test this quickly. Naively, I would expect a large depedence on Ndata.]

Testing the error convolved likelihood approximation.— [TO DO: Comment from HW: This is a very technical aspect: it should be summarized in 1-2 sentences; you neither have to provide code documentation, nor document effort. The reader wants the upshot.] [TO DO: Jo doesn't like subsub(sub?)sections... Remove.] In absence of distance (modulus) errors our approximation for the likelihood, which is the model probability convolved with the measurement uncertainties in Equation 15, is equal to the true likelihood. In case there *are* distance modulus errors, this likelihood links the range of possible velocities (specified by the measurement errors in line-of-sight velocity, proper motion and distance modulus) to a fixed but slightly wrong position, as we ignore the distance error in the position. As the link between position and velocity provides the information about the potential, this will lead to systematic biases in the parameter recovery the larger the distance error becomes. In Test 6.2 in Table 3 and Figure 11 we investigate the capabilities of Equation 15 with and without distance modulus errors.
The left column of panels in Figure 11 shows how well the approximation works in the absence of distance errors. There seemed to be no biases in the parameter recovery, independent of the size of the proper motion error. Overall the standard errors on the recovered parameters are quite small (a few percent at most for 10,000 stars), which demonstrates that, if we perfectly knew the measurement errors, we still could get very precise constraints on the potential. The constraints also get tighter the smaller the proper motion error becomes. We found that for $\delta\mu = 1$ mas yr^{-1} the precision of the recovered parameters reduce by $\sim$ half compared to $\delta\mu = 5$ mas yr^{-1}. [TO DO: Comment from HW: This seems to be a (sensible) statement about the impact of the errors. Why is it under the heading of testing an approximation?]
The right column of panels in Figure 11 demonstrates the failure of our adopted likelihood approximation in the case of large distance modulus errors. The larger the $\delta(m-M)$, the wronger the recovered parameters become: The systematic biases can get many SEs large. We find however that in case of $\delta(m-M) \leq 0.2$ mag (if also $\delta\mu \leq 2$ mas yr^{-1} and a maximum distance of $r_{\max} = 3$ kpc, see Test 6.2 in Table 3) the parameters can still be recovered within 2 SEs. For most model parameters (except $\ln(\sigma_{z,0}/200\ \mathrm{km\ s}^{-1})$, as shown in the figure, and $\ln(h_R/8\ \mathrm{kpc})$) even $\delta(m-M) \leq 0.3$ mag still gives biases smaller than 2 SEs. This corresponds to a relative distance error of $\sim$ 10%. This encourages us that for smaller distance modulus errors we really could use our likelihood approximation in Equation 15, which is computationally cheaper than a proper treatment, also on real data sets.

We found that in case we perfectly knew the measurement errors (and the distance error is negligible), the convolution of the model probability with the measurement errors gives precise and accurate constraints on the model parameters - even if the error itself is quite large. [TO DO: That statement should be the last, concluding sentence of one of the previous sections. Then its fresh in the reader's mind, and does not need repeating.]

Underestimation of the proper motion error.— Now we investigate what would happen if the quoted measurement errors, e.g. the proper motion errors, were actually smaller than the true errors. Figure 13 shows the case for two different stellar populations and an error underestimation of 10% and 50%.
Overall the parameter recovery gets worse the larger the proper motion error and the stronger the underestimation. The relation between the bias due to error misjudgment and the size of the proper motion error seems to be linear.
For the recovery of the isochrone potential scale length b the hotness of the population does not matter (see lower

left panel in Figure 13). The circular velocity $v_{\rm circ}(R_\odot)$ is, as always, better measured by cooler than by hotter populations (see upper left panel in Figure 13).

We find that the recovery of the qDF parameters on the other hand is more strongly affected by the misjudgment of the velocity error for *cooler* stellar popluations. The measured velocity dispersion is the convolution of the intrinsic dispersion with the measurement errors. If the proper motion error is underestimated, the deconvolved velocity dispersion is larger than the intrinsic velocity dispersion and the relative difference is bigger for a cooler population (see upper right panel for $\sigma_{z,0}$ in Figure 13). The intrinsic velocity dispersion is also cooler at larger radii than at smaller radii, therefore the deconvolved dispersion is overestimated more strongly at large R and the velocity dispersion scale length will be overestimated as well (see lower left panel for $h_{\sigma,z}$ in Figure 13). We get analogous results for the qDF parameters $\sigma_{R,0}$ and $h_{\sigma,R}$. The recovery of the tracer density scale length h_R is not affected by the misjudgment of velocity errors.

The most important and encouraging result from Figure 13 is, that for an underestimation of 10% the bias is still $\lesssim$ 2 sigma for 10,000 stars [TO DO: Check] - even for proper motion errors of almost 3 mas/yr.

[TO DO: Comment from Jo: Always use 'uncertainty' when describing how ou deal with the errors. 'Error' means the actual error (difference between observed and true).]

3.5. *The Impact of Deviations of the Data from the Idealized qDF*

Our modelling approach assumes that each MAP follows a quasi-isothermal distribution function, qDF. In this Section we explore what happens if this idealization does not hold. We investigate this issue by creating mock data sets (Figure 14) that are drawn from two distinct qDFs of different temperature, and analyze the composite mock data set by fitting a single qDF to it. These results are illustrated in Figures 15 and 16. Following the observational evidence, MAPs with cooler qDFs also have longer tracer scale lengths. In the first set of test, we choose qDFs of widely different temperatures and vary their relative fraction (dubbed *Examples 1a/b* in Figure 15 and Test 7 in Table 3); in the second set of tests (*Examples 2a/b* in Figure 16 and Test 7in Table 3), we always mix mock data points from two different qDFs in equal proportion, but vary by how much the qDF's temperatures differ.

The first set of tests mimics a DF that has wider wings or a sharper core in velocity space than a qDF (Figure 14). The second test could be understood as mixing neighbouring MAPs due to large bin sizes or abundance measurement errors.

It is worth considering the impact of the DF deviations on the recovery of the potential and of the qDF parameters separately. We find from Example 1 that the potential parameters can be better and more robustly recovered, if a mock-data MAP is polluted by a modest fraction ($\lesssim$ 30%) of stars drawn from a much cooler qDF with a longer scale length, as opposed to the same pollution of stars drawn from a hotter qDF with a shorter scale length.

When considering the case of a 50/50 mix of contributions from different qDFs in Example 2, there is a systematic, but only small, error in recovering the potential parameters, monotonically increasing with the qDF parameter difference; in particular for fractional differences in the qDF parameters of $\lesssim$ 20% the systematics are insignificant even for samples sizes of 20,000, as used in the mock data.

Overall, mock data drawn from a cooler DF always seem to give tighter constraints on the circular velocity at the Sun [TO DO: Make sure that Sun is written everywhere with a capital S.], because the rotation curve can be constrained easier if more stars are on near-circular orbits. But we found the recovered $v_{\rm circ}(R_\odot)$ not always to be unbiased at the implied precision.

The recovery of the effective qDF parameters, in light of non-qDF mock data is quite intuitive: the effective qDF temperature lies between the two temperatures from which the mixed DF of the mock data was drawn; in all cases the scale length of the velocity dispersion fall-off, $h_{\sigma,R}$ and $h_{\sigma,z}$, is shorter, because the stars drawn form the hotter qDF dominate at small radii, while stars from the cooler qDF (with its longer tracer scale length) dominate at large radii. The recovered tracer scale lengths, h_R vary smoothly between the input values of the two qDFs that entered the mix of mock data, with again the impact of contamination by a hotter qDF (with its shorter scale length in this case) being more important. Overall, we find that the potential inference is quite robust to modest deviations of the data from the assumed DF.

3.6. *The Implications of a Gravitational Potential not from the Space of Model Potentials*

We now explore what happens when the mock data were drawn from one axisymmetric potential family, here `MW14-Pot`, and is then modelled considering potentials from only another axisymmetric family, here `KKS-Pot` (compare the second and fourth panel in Figure 1). In the analysis we assume the circular velocity at the Sun to be fixed and known [TO DO: Comment from Hans-Walter: Do we have reason to believe that this very restrictive assumption does not qualitatively impact our upshot (quantitative differences are OK).] and only fit the parametric potential form. The results are shown in Figure 18.

The reference potential parameters [TO DO: Comment from HW: What does "reference" mean here exactly? Is this an independent exercise, to ask which parameters are expected when fitting potential to potential? (I don't know, what he means...)] of the `KKS-Pot` in Table 1 were found by adjusting the 2-component Kuzmin-Kutuzov Stäckel potential by Batsleer & Dejonghe (1994) such that it generates radial and vertical force profiles similar to the `MW14-Pot` from Bovy (2015) (dotted gray lines in Figure 18). We then run *RoadMapping* using these "inconsistent" families of gravitational potentials, and find a good fit to the data in configuration space (see Figure 17). The results from *RoadMapping* analysis for the potential shown in Figure 18, red for a `hot` mock data MAP and blue for a `cool` MAP, give an comparable good or even better agreement with the true potential than the (by-eye) fit directly to the potential: especially the force contours, to which the orbits are sensitive, and the rotation curve are very tightly constrained and reproduce the true potential even outside of the observed volume of the mock tracers. This demonstrates that *RoadMapping*

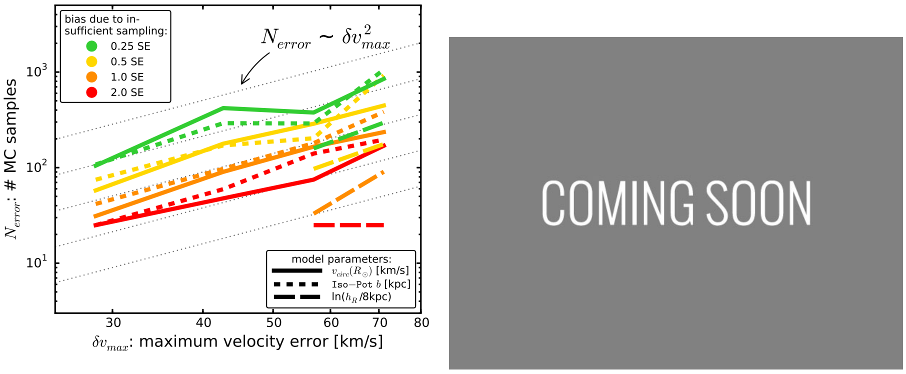

(a) $N_* = 10,000$

(b) $N_* = 5,000$

Figure 10. Number of Monte Carlo (MC) samples $N_{\rm error}$ needed for the numerical error convolution in Equation 15, given the maximum velocity error $\delta v_{\rm max}$ in the sample to reach a given accuracy. An insufficient sampling of the convolution integral leads to systematic biases in the reconstruction of the true model parameters. The size of the bias is color coded as indicated in the legend and is given in units of the standard error (SE). The model parameters, marked by different symbols, have different sensitivities to the numerical inaccuracy of the error convolution, therefore the range in $N_{\rm error}$ for the same given bias. Here we assume that the distance error is zero and the proper motion error $\delta\mu$ translates to a velocity error according to Equation 16 and $\delta v_{\rm los} \ll \delta v_{\rm max}$. All model parameters are listed in Table 3 as Test 6.1. The number of MC samples needed increases with the velocity error as $N_{\rm error} \propto (\delta v_{\rm max})^2$, as can be seen especially well in the inset figure for the potential parameter $v_{\rm circ}(R_\odot)$. All lines are fits of this functional form to each four points derived for a given model parameter (symbol) and bias (color). The large scatter in the points comes from low number statistics and errors introduced by linear interpolation of the bias vs. $N_{\rm error}$ relation found from the analyses. [TO DO: rename $h_{\sigma R}$ to $h_{\sigma,R}$, σ_R to $\sigma_{R,0}$ and analogous for z] [TO DO: some of the 25 MC sample analyses have to be re-done. (Currently running on cluster.)] [TO DO: Rewrite caption. I changed the whole plot.] [TO DO: Replace right plot with new plot with $N_* = 5,000$] [TO DO: Use N_* everywhere where applicable] [TO DO: Intriduce N_* somewhere.]

fitting inferres a potential that in its actual properties resembles the input potential for the mock data as closely as possible, given the differences in functional forms.
The density contours are less tightly constrained than the forces, but we still capture the essentials: the `hot` MAP from Table 2 constrains the halo; especially at smaller radii it is equally good or better than the `cool` MAP. The `cool` MAP gives tighter constraints on the halo in the outer region and recovers the disk better than the `hot` MAP. This is in concordance with expectations as the `cool` MAP has a longer tracer scale length and is more confined to the disk than the `hot` MAP and therefore also probes the Galaxy in these regions better.
Overall the best fit disk is less dense in the midplane than the true disk.

Figure 19 compares the true qDF parameters with the best fit parameters for this case. While tracer scale length and radial velocity dispersion profile are very well recovered, we misjudge the radial profile of the vertical velocity dispersion as $\sigma_{0,z}$ and $h_{\sigma,z}$ are both underestimated, which leads to a steeper profile and a lower dispersion around the Sun.

4. DISCUSSION AND SUMMARY

[TO DO: Introduce DF somewhere - use DF wherever we don't need qDF.]
[TO DO: Compare these sections with the results. Points should be made detailed in the results section and short here in the discussion. Says Hans-Walter.]

Recently implementations of action DF-based modelling of 6D data in the Galactic disk have been put forth, in part to lay the ground-work fo Gaia (Bovy & Rix 2013; McMillan & Binney 2013; Piffl et al. 2014; Sanders & Binney 2015).
We present *RoadMapping*, an improved implementation of the dynamical modelling machinery of Bovy & Rix (2013), to recover the potential and orbit distribution function of stellar MAPs within the Galactic disk. In this work we investigated the capabilities, strengths and weaknesses of *RoadMapping* by testing its robustness against the breakdown of some of its assumptions - for well defined, isolated test cases using mock data. Overall the method works very well and is reliable, even when there are small deviations of the model assumptions from the real world Galaxy.
RoadMapping applies a full likelihood analysis and is statistically well-behaved. It allows for a straightforward implementation of different potential model families and a flexible number of free fit parameters in potential and DF. It also accounts for selection effects by using full 3D selection functions (given some symmetries). *RoadMapping* is an asymptotically normal, unbiased estimator and the precision of parameter recovery increases by $1/\sqrt{N}$ with the number of stars.

Computational speed: Large data sets in the age of Gaia require more, and more accurate, likelihood evaluations for more flexible models. To be able to deal with these increased computational demands and explore larger parameter spaces, we sped up the code by combining a nested grid approach with MCMC and by faster action calculation using the Stäckel (Binney 2012) interpolation grid by Bovy (2015). However, application of *RoadMapping* to millions of stars simultaneously with acceptable accuracy will still be a task for supercomputers and calls for even more improvements and speed-up in the fitting machinery.

Properties of the data set: We could show that *RoadMapping* can provide potential and DF parameter estimates that are very accurate (i.e. unbiased) and precise in the the limit of large datasets, as long as the modelling assumptions are fulfilled. We also found that the location of the survey volume matters little. At

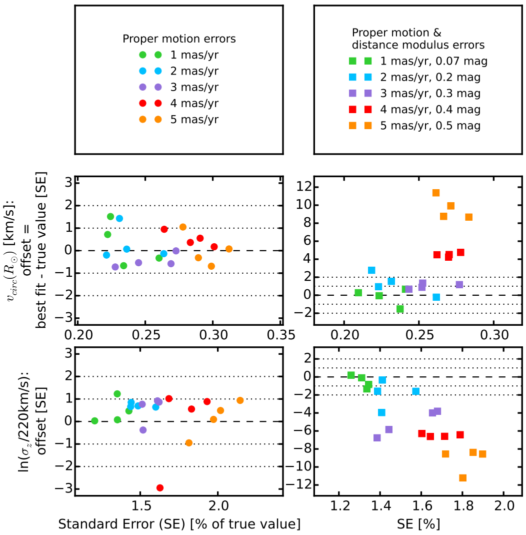

Figure 11. Parameter recovery using the approximation for the measurement error convolved likelihood in Equation 15. All model parameters used to create the mock data sets analyzed for this figure are given as Test 6.2 in Table 3. The mock data sets in the left panels have only errors in line-of-sight velocity and proper motions, while the data sets in the right panels also have distance modulus errors, as indicated in the legends in the first row. The size of the error is color coded. The other panels plot the offset of the recovered model parameter to the true parameter vs. the relative standard error for two of the seven model parameters, the potential parameter $v_{\text{circ}}(R_\odot)$ and qDF parameter $\sigma_{z,0}$. For data sets with proper motion error errors $\delta(m-M) \leq 3$ mas yr^{-1} Equation 15 was evaluated with $N_{\text{error}} = 800$, for $\delta(m-M) > 3$ mas yr^{-1} we used $N_{\text{error}} = 1200$. In the absence of distance errors Equation 15 gives unbiased results. For $\delta(m-M) \geq 3$mas yr^{-1} (which corresponds in this test to $\delta v_{\max} \lesssim 43$ km s^{-1}, see Equation 16) however biases of several sigma are introduced as Equation 15 is only an approximation for the true likelihood in this case. [TO DO: rename σ_z to $\sigma_{z,0}$] [TO DO: Show b instead of σ_z and don't comment the small offset.] [TO DO: Incorporate legends within the bottom panels, with only one point (numpoints=1)] [TO DO: Use viridis color map] [TO DO: Add the additional analyses I did in the left column, e and f.]

Figure 12. [TO DO: This should be a figure that plots precision (SE) vs. proper motion error for a hot and a cool population (for no distance error). This is to demonstrate the effect of measurement errors in general.]

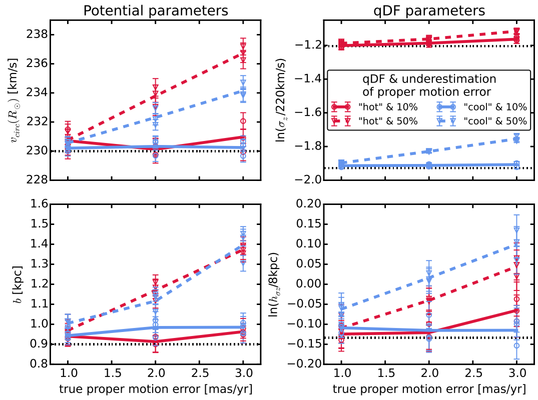

Figure 13. Effect of a systematic underestimation of proper motion errors in the recovery of the model parameters. The true model parameters used to create the mock data are summarized as Test 6.3 in Table 3, four of them are given on the y-axes and the true values are indicated as black dashed lines. The velocities of the mock data were perturbed according to Gaussian errors in the RA and DEC proper motions as indicated on the x-axis. The circles and triangles are the best fit parameters of several mock data sets assuming the proper motion uncertainty, with which the model probability was convolved, was underestimated in the analysis by 10% or 50%, respectively. The error bars correspond to 1 sigma confidence. The lines connect the mean of each two data realisations and are just to guide the eye. [TO DO: rename $h_{\sigma z}$ to $h_{\sigma,z}$, σ_z to $\sigma_{z,0}$] [TO DO: Potential and/or population names in typewriter font]

given sample size, the volume over which the data are sampled also matters little, if the modelling assumptions are fulfilled. are fulfilled. Concerning the *shape* of the survey volume, a large radial *and* vertical coverage is best, because in the axisymmetric regime the azimuthal coverage does not matter.

Stellar populations of different scale length and temperature probe different regions of the Galaxy (Bovy & Rix 2013). But there is no easy rule of thumb for which survey volume and stellar population which potential and DF parameter is constrained best.

Surprisingly, (cf. Rix & Bovy 2013) *RoadMapping* seems to be very robust against misjudgments in the selection function of the data. We speculate that this is because missing stars in the data set do not affect the connection between a star's velocity and position, which is given by the potential. Much of the information about the potential profile is stored in the rotation curve, but we find that even when when we do not include measurements of tangential velocities in the analysis, small misjudgments of the incompleteness do not affect the potential recovery.

[TO DO: Comment from HW: Author: rix Subject: This paragraph shouldbe 1 or 2 sentences, following the first paragraph on "Sample/Data Properties". This –at the moments –reads to bequite confusing. I don't quite get whatthe "upshot" is; thereistechnical detai on N_{error} [enought to say it's expensive]; and, as noted earlier; I don't understand why theerror convolution for a nearbydata point needs to know about $\delta v_{\max}$] Properly convolving the likelihood with measurement errors is computational very expensive. By ignoring positional errors and only including distance errors as part of the velocity error, we can drastically reduce the computational costs. For stars within 3 kpc from the

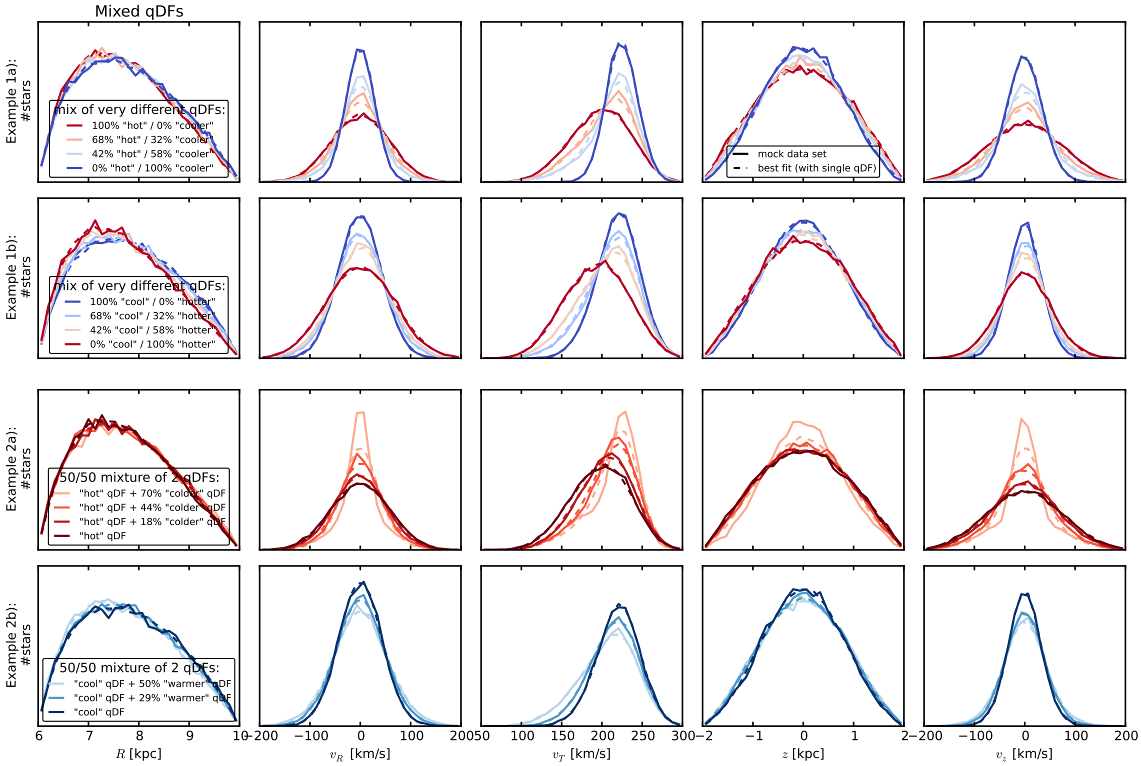

Figure 14. Distribution of mock data, created by mixing stars drawn from two different qDFs (solid lines), and the distribution predicted by the best fit of a single qDF and potential to the data (dashed lines). The model parameters to create the mock data (solid lines) are given in Table 3 as Test 7, and the qDF parameters referenced in the figure's legend are given in Table 2. The corresponding single qDF best-fit curves (dashed lines) were created by drawing mock data from the best fit parameters found in Figures 15 and 16. *Example 1:* Distribution of mock data drawn from a superposition of two very different (but fixed) qDFs at varying mixing rates. *Example 2:* Mock data distribution of two MAPs that were mixed at a fixed rate of 50%/50%, but the difference of the qDF parameters of one MAP was varied with respect to the qDF parameters of the other MAP by X% (see Table 2). The data sets are color coded in the same way as the corresponding analyses in Figures 15 and 16. This figure demonstrates how mixing two qDFs can be used as a test case for changing the shape of the DF to not follow a pure qDF anymore, e.g. by adding wings or slightly changing the radial density profile. When comparing the mock data and best fit distribution, we see that especially for the most extreme deviations it becomes obvious that a single qDF is a bad assumption for the stars' *true* DF. [TO DO: Potential and/or population names in typewriter font] [TO DO: include X somehow in figure to explain it better. Jo didn't understand what I meant by it in this caption.] [TO DO: These are really many panels. Try to remove some.]

sun this approximation works well for distance errors of $\sim$ 10% or smaller. The number of MC samples needed for the error convolution using MC integration scales by $N_{\text{error}} \propto (\delta v_{\max})^2$ with the maximum velocity error at the edge of the sample. If we did not know the true size of the proper motion measurement errors perfectly, we can only reproduce the true model parameters to within $\lesssim$ 2 sigma [TO DO: Check???] as long as we do not underestimate it by more than 10% and for proper motion errors $\lesssim$ 2 mas yr^{-1}.

Deviations from the qDF Assumption: Our modelling is founded on the assumption, that we can identify *a priori* sub-components of the Galactic disk that follow a qDF (e.g., by considering MAPs). There are two reasons why any chosen sub-sample of stars (here a MAP) may not be well described by any qDF. Either, because nature is more complex, or because even if perfect MAPs would be well described by qDFs finite abundance errors would mix MAPs. We have considered both cases. [TO DO: Comment from HW: it feels to me that this is the 3rd time you said this.It's OK to say, but in1 line at most.]

In Example 1 in §3.5 we investigated how well we can recover the potential, if this assumption was not perfectly satisfied, i.e., the MAP's true DF does not perfectly follow a qDF. We considered two cases: a) a hot DF, that has less stars at small radii and more stars with low velocities than predicted by the qDF (reddish data sets in Figure 14), or b) a cool DF that has broader velocity dispersion wings and less stars at large radii than predicted by the qDF (bluish data sets). We find that case a) would give more reliable results for the potential parameter recovery, but in both cases biases are small if the contamination is less than [TO DO: CHECK].

If we assumed that the distribution of stars from one MAP is caused by radial migration away from the initial location of star formation, it would more likely that the qDF overestimates the true number of stars at smaller radii than underestimating it at larger radii. [TO DO: Is this actually a sensible argument??? Jo is not convinced that this is right.]

Following this, focusing the analysis especially on hotter MAPs could be an advisable way to go in the future, if there is doubt that the stars truly follow the qDF.

Another critical point is the binning of stars into MAPs depending on their metallicity and α abundances. Example 2 in §3.5 could be understood as a model scenario for decreasing bin sizes in the metallicity-α plane when sorting stars in different MAPs, assuming that there is a

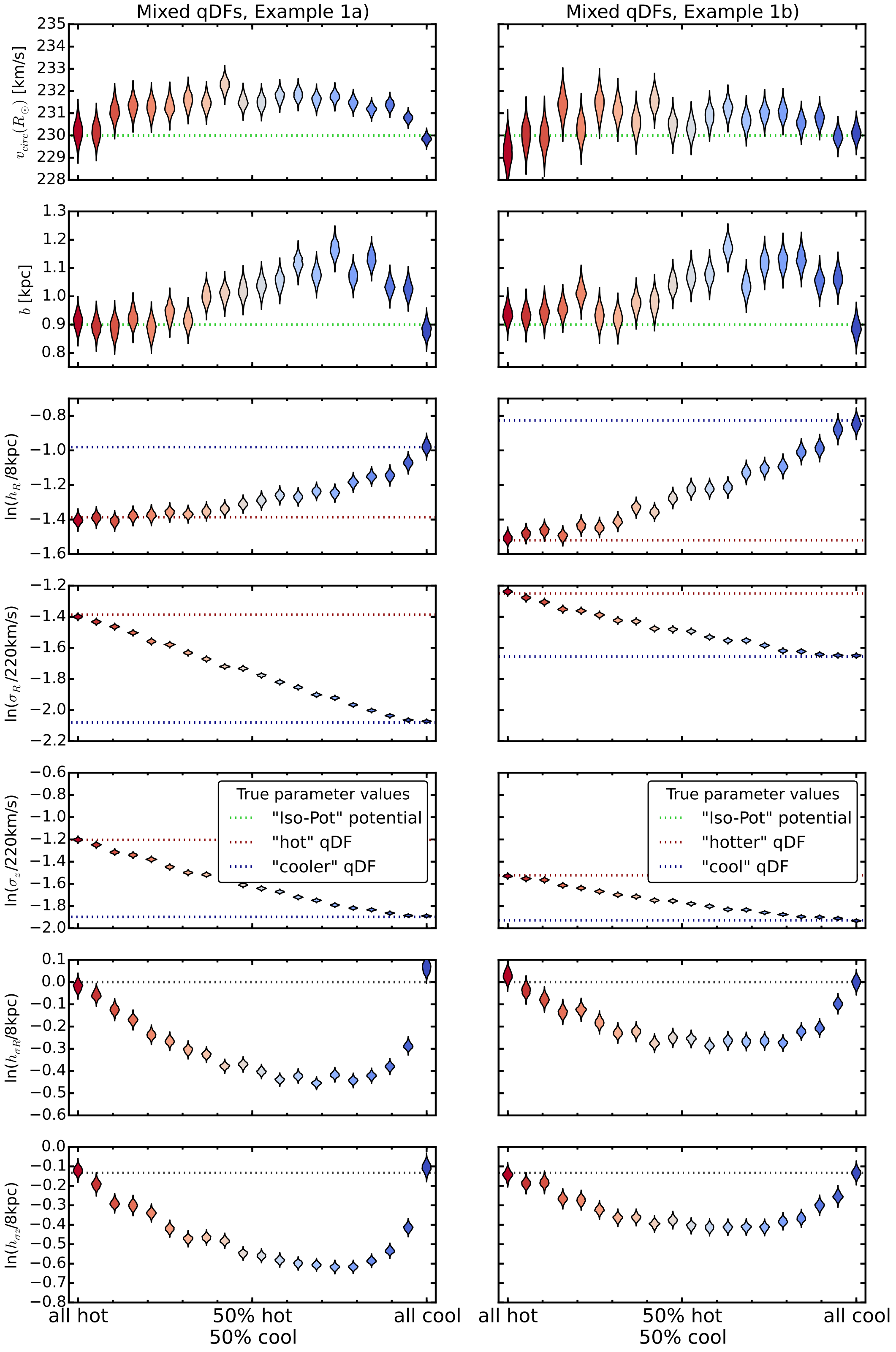

Figure 15. The dependence of the parameter recovery on degree of pollution and temperature of the stellar population. To model the pollution of a hot stellar population by stars coming from a cool population and vice versa, we mix varying amounts of stars from two very different populations, as indicated on the X-axis. The composite mock data set is then fit with one single qDF. The violins represent the marginalized likelihoods found from the MCMC analysis. *Example 1a* (*Example 1b*) in the left (right) panels mixes the `hot` (`cool`) MAP with the `cooler` (`hotter`) MAP in Table 2. All model parameters used to create the mock data are given in Test 7, *Example 1a) & b)* in Table 3. Some mock data sets are shown in Figure 14, first two rows, in the same colors as the violins here. We find that a hot population is much less affected by pollution with stars from a cooler population than vice versa. [TO DO: rename $h_{\sigma R}$ to $h_{\sigma,R}$, σ_R to $\sigma_{R,0}$ and analogous for z] [TO DO: Potential and/or population names in typewriter font] [TO DO: Comment from Jo: I feel like just showing one of these examples might be clearer, because they essentially demonstrate the same thing.] [TO DO: Remove σ_R and $h_{\sigma,R}$ panels. Then make two columns with only one expample, potential and DF parameters separately]

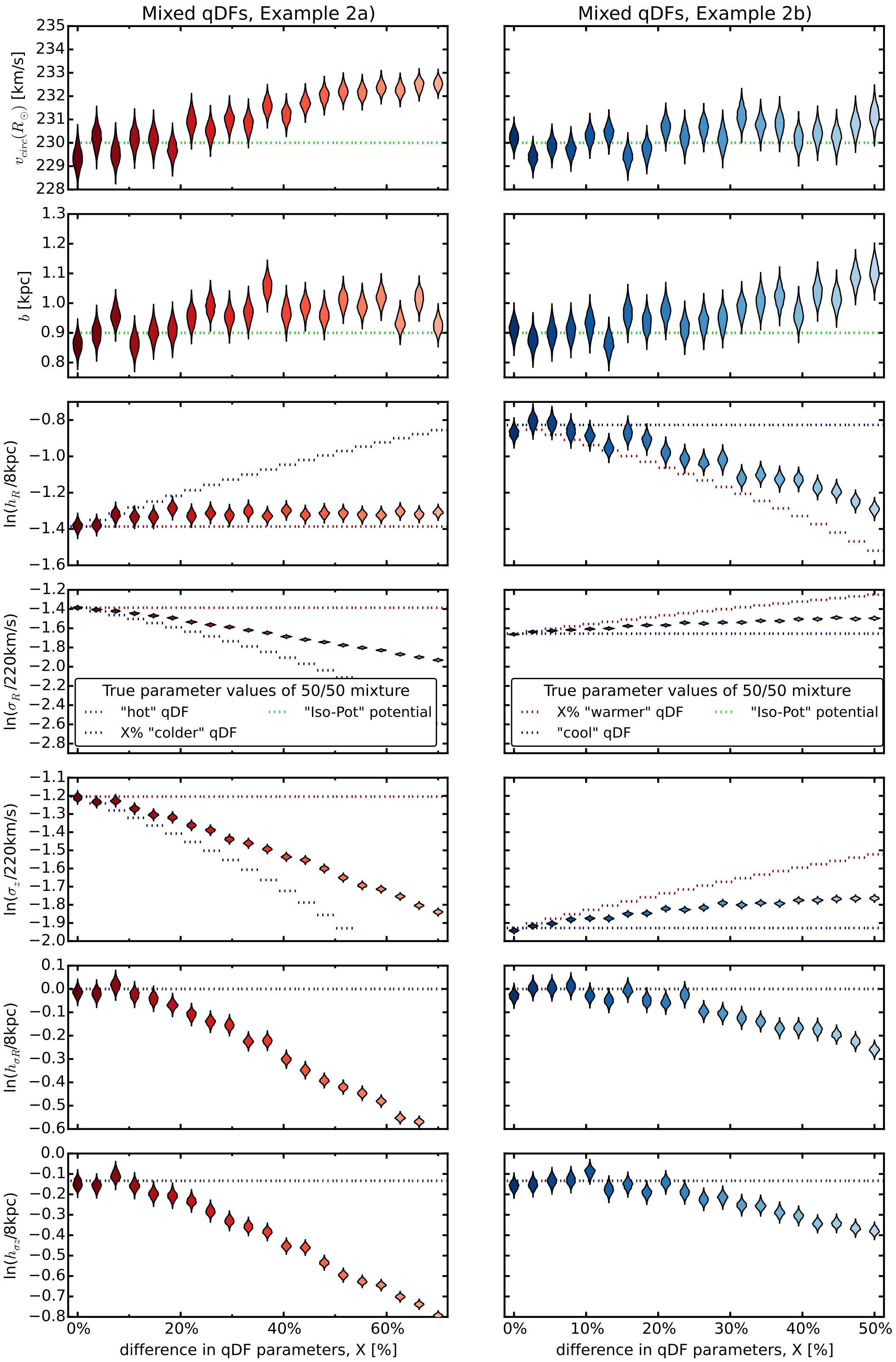

Figure 16. (Caption on next page.)

Figure 16. The dependence of the parameter recovery on the difference in qDF parameters of a 50%/50% mixture of two stellar populations and their temperature. Half of the star in each mock data set in *Example 2a* (*Example 2b*) was drawn from the `hot` (`cool`) qDF in Table 2, and the other half drawn from a `colder` (`warmer`) population that has $X\%$ smaller (larger) $\sigma_{R,0}$ and $\sigma_{z,0}$ and $X\%$ larger (smaller) h_R. Each composite mock data set is then fitted by a single qDF and the marginalized MCMC likelihoods for the best fit parameters are shown as violins. The model parameters used for the mock data creation are given as Test 7, *Example 2a) & b)* in Table 3. Some mock data sets are shown in figure 14, last two rows, where the distributions have the same colors as the corresponding best fit violins here. By mixing MAPs with varying difference in their qDF parameters, we model the effect of bin size in the [Fe/H]-[α/Fe] plane when sorting stars into different MAPs: The smaller the bin size, the smaller the difference in qDF parameters of stars in the same bin. We find that the bin sizes should be chosen such that the difference in qDF parameters between neighbouring MAPs is less than 20%. [TO DO: rename $h_{\sigma R}$ to $h_{\sigma,R}$, σ_R to $\sigma_{R,0}$ and analogous for z] [TO DO: Potential and/or population names in typewriter font]

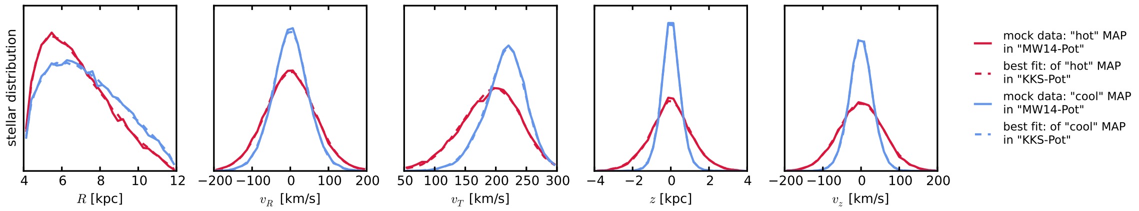

Figure 17. Comparison of the distribution of mock data in configuration space created in the `MW14-Pot` potential (solid lines) with a `hot` (red) and `cool` (blue) MAP (Test 8 in Table 3), and the best fit distribution using a `KKS-Pot` potential (dashed lines). The best fit potentials are shown in Figure 18 and the corresponding best fit qDF parameters in Figure 19. The best fit [TO DO: Continue Caption, Jo suggests add something about the fit being good.] [TO DO: Potential and/or population names in typewriter font]

smooth variation of qDF within the metallicity-α plane and each MAP indeed follows a qDF. We find that, in the case of 20,000 stars in each bin, differences of 20% in the qDF parameters of two neighbouring bins can still give quite good constraints on the potential parameters. We compare this with the relative difference in the qDF parameters in the bins in Figure 6 of Bovy & Rix (2013), which have sizes of [Fe/H] $= 0.1$ dex and Δ[α/Fe] $= 0.05$ dex. It seems that these bin sizes are large enough to make sure that $\sigma_{R,0}$ and $\sigma_{z,0}$ of neighbouring MAPs do not differ more than 20%. Figure 15 and 16 suggest that especially the tracer scale length h_R needs to be recovered to get the potential right. For this parameter however the bin sizes in Figure 6 of Bovy & Rix (2013) might not yet be small enough to ensure no more than 20% of difference in neighbouring h_R. This is especially the case in the low-α ([α/Fe] $\lesssim 0.2$), intermediate-metallicity ([Fe/H] ~ -0.5) MAPs, which where however not used in the dynamical modelling by Bovy & Rix (2013). The above is valid for 20,000 stars per MAP. In case there are less than 20,000 stars in each bin the constraints are less tight and due to Poisson noise one could also allow larger differences in neighbouring MAPs while still getting reliable results.

[TO DO: Include the following comments by Jo somewhere: This is a general approach of fitting action-based disk DFs for getting the potential. The qDF is a specific example that we use in this paper. In futures studies different forms of DFs might be fitted to data. That the results are quite robust to the form of the DF not entirely correct motivates this further.]

Gravitational Potential beyond the Parameterized Functions Considered: [TO DO: Comment from HW: In style and contentthis seems verysimilar tothe RESULTSsection. We should eitherdrastically shorten the text in the results section (probably not), or here.] In the long run *RoadMapping* should incorporate a family of gravitational potential models that can reproduce the essential features of the MW's true mass distribution. While our fundamental assumption of the Galaxy's axisymmetry is at odds with the obvious existence of non-axisymmetries in the MW, we will not dive into investigating this implications in this paper. Instead we test how a misjudgment of the parametric potential form affects the recovery by fitting a potential of Stäckel form (Batsleer & Dejonghe 1994) to mock data from a different potential family with halo, bulge and exponential disk. The recovery is quite successful and we get the best fit within the limits of the model. However, even a strongly flattened Stäckel potential component has difficulties to recover the very flattened mass distribution of an exponential disk. This leads to misjudgment of the qDF parameters describing the vertical action distribution, $\sigma_{z,0}$ and $h_{\sigma,z}$. As the qDF parameter $\sigma_{z,0}$ corresponds to the physical vertical velocity dispersion at the sun, a comparison with direct measurements could be a valuable cross-checking reference. [TO DO: This might not be true. For isochrone and Staeckel potential I get this behaviour, but not for the MW14-Pot!!! Might be, because it's not separable??? Check!!!] [TO DO: best to simply remove it...] In case of as many as 20,000 stars we should therefore already be able to distinguish between different potential models.

The advantage of using a Stäckel potential with *RoadMapping* is firstly the exact and fast action calculation via the numerical evaluation of a single integral, and secondly that the potential has a simple analytic form, which greatly speeds up calculations of forces and frequencies (as compared to potentials in which only the density has an easy description like the exponential disk). A superposition of several simple Kuzmin-Kutuzov Stäckel components can successfully produce MW-like rotation curves (see Batsleer & Dejonghe (1994), Famaey & Dejonghe (2003) and Figure 18) and one could think of adding even more components for more flexibility, for example a small roundish component for the bulge. [TO DO: Comment by Jo: In a sense the two approaches (a) using the Staeckel action approximation with a MW like potential and (b) using a Staeckel potential directly are dong the same thing (approximating the true potential as a Staeckel potential). The question is which is best.]

The potential model used by Bovy & Rix (2013) had

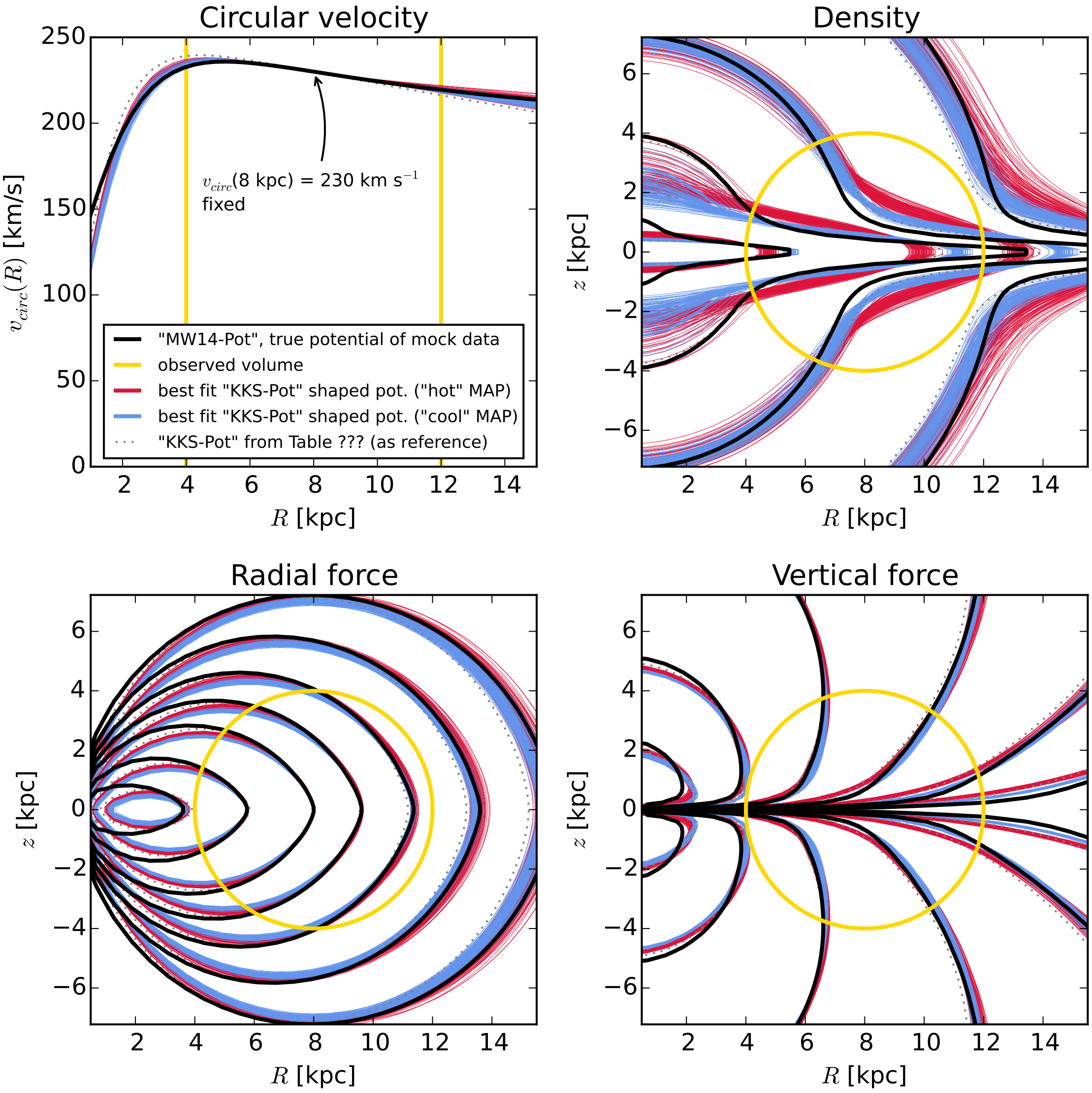

Figure 18. Recovery of the gravitational potential if the assumed potential model (`KKS-Pot` with fixed $v_{\rm circ}(R_\odot)$) and the true potential of the (mock) stars (`MW14-Pot` in Table 1) is slightly different. We show the circular velocity curve, as well as contours of equal density, radial and vertical force in the R-z-plane, and compare the true potential with 50 [TO DO: CHECK] sample potentials drawn from the posterior distribution function found with the MCMC for a `hot` (red) and a `cool` MAP (blue). All model parameters are given as Test 8 in Table 3. [TO DO: Do more analyses???] [TO DO: fancybox Legend] [TO DO: Potential and/or population names in typewriter font] [TO DO: Reference correct Table in Plot - don't forget!] [TO DO: Redo whole analysis with vcirc not being fixed (HW is not sure if this really doesn't make a difference.] [TO DO: Comment from Jo: Maybe better with twice as many contour levels? Now not that many within the yellow curve.]

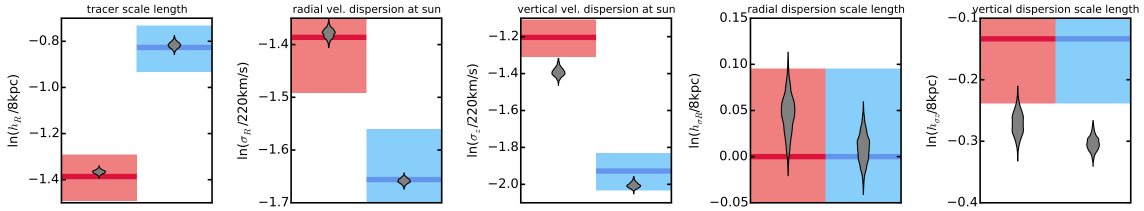

Figure 19. Recovery of the qDF parameters for the case where the true and assumed potential deviate from each other (Test 8 in Table 3). The thick red (blue) lines represent the true qDF parameters of the `hot` (`cool`) qDF in Table 2 used to create the mock data, surrounded by a 10% error region. The grey violins are the marginalized likelihoods for the qDF parameters found simultaneously with the potential constraints shown in Figure 18. [TO DO: rename $h_{\sigma R}$ to $h_{\sigma,R}$, σ_R to $\sigma_{R,0}$ and analogous for z]

only two free parameters (disk scale lentgh and halo contribution to $v_{\rm circ}(R_\odot)$. To circumvent the obvious disadvantage of this being at all not flexible enough, they fitted the potential separately for each MAP and recovered the mass distribution for each MAP only at that radius for which it was best constrained - assuming that MAPs of different scale length would probe different regions of the Galaxy best. Based on our results in Figure 18 this seems to be indeed a sensible approach [TO DO: Check that this is indeed the case - it is not clear to me from the plot. ???].

We suggest that combining the flexibility and computational advantages of a superposition of several Stäckel potential components with probing the potential in different regions with different MAPs as done by Bovy & Rix (2013), could be a promising approach to get the best possible constraints on the MW's potential.

Different Modelling Approaches using Action-based Distribution Functions: We have focussed for the time being on MAPs for a number of reasons: First, they seem to permit simple DFs (Bovy et al. 2012b,c,d), i.e., approximately qDFs (Ting et al. 2013). Second, all stars, e.g., those from different MAPs, must orbit in the same potential. Therefore each MAP will and can yield quite different DF parameters; but each MAP will also provide a (statistically) independent estimate of the potential parameters. At the same time—if all is well—those potential parameters, derived from different MAPs, should be mutually consistent. In some sense, this approach focusses on constraining the potential, treating the DF parameters as nuisance parameters.

The main drawback is that we have many astrophysical reasons that the DF properties (for reasons of galaxy evolution and chemical evolution) are astrophysically linked between different MAPs. Ultimately, the goal is to do a fully consistent chemodynamical model that simultaneously fits the potential and DF($\boldsymbol{J}$, [X/H]) simultaneously (where [X/Fe] denotes the full abundance space) with a full likelihood analysis. This has not yet been attempted here, because the behaviour is quite complex.

Since the first application of *RoadMapping* by Bovy & Rix (2013) there have been two similar efforts to constrain the Galactic potential and/or orbit distribution using action-based distribution functions:

Piffl et al. (2014) fitted both potential and a $f(\boldsymbol{J})$ to giant stars from the RAVE survey (Steinmetz et al. 2006) and the vertical stellar number density profiles in the disk by Jurić et al. (2008). They did not include any chemical abundances in the modelling. Instead, they used a superposition of action-based DFs to describe the overall stellar distribution at once: a superposition of qDFs for cohorts in the thin disk, a single qDF [TO DO: CHECK] for the thick disk stars and an additional DF for the halo stars. Taking proper care of the selection function requires a full likelihood analysis and the calculation of the likelihood normalisation is computational expensive. Piffl et al. (2014) choose to circumvent this problem by directly fitting a) histograms of the three velocity components in eight spatial bins to the velocity distribution predicted by the DF and b) the vertical density profile predicted by the DF to the profiles by Jurić et al. (2008). The vertical force profile of their best fit mass model nicely agrees with the results from Bovy & Rix (2013) for $R > 6.6$ kpc. The disadvantage of their approach is, that by binning the stars spatially, a lot of information is not used.

Sanders & Binney (2015) have focussed on understanding the abundance-dependence of the DF, relying on a fiducial potential. They developed extended distribution functions, i.e., functions of both actions and metallicity for a superposition of thin and thisk disk, each consisting of several cohorts described by qDFs, a DF for the halo, a functional form of the metallicity of the interstellar medium at the time of birth, and a simple prescription for radial migration. They applied a full likelihood analysis accounting for selection effects and found a best fit for the eDF in a fixed fiducial potential by Dehnen & Binney (1998) to the stellar phase-space and metallicity [TO DO: CHECK] data of the Geneva-Copenhagen Survey (Nordström et al. 2004; Holmberg et al. 2009) and the stellar density curves by Gilmore & Reid (1983). Their best fit predicted the velocity distribution of SEGUE G dwarfs quite well, but had biases in the metallicity distribution, which they accounted to being a problem with the SEGUE metallcities.

We know that real galaxies, including the Milky Way, are not axisymmetric. Using N-body models, we will explore in a subsequent paper what when data from a non-axisymmetric system get interpreted through axisymmetric modelling.

[TO DO: Comment from Jo: Maybe we also want a conclusion with a simple bullet-point list of the main conclusions discussed in detail in the Discussion section.]

5. ACKNOWLEDGMENTS

The authors thank Glenn van de Ven for suggesting the use of Kuzmin-Kutuzov Stäckel potentials in this case study. [TO DO: What else do we to have acknowledge???]

APPENDIX

Influence of wrong assumptions about incompleteness of the data parallel to the Galactic plane

In §3.3 we found a striking robustness of the *RoadMapping*modelling approach against wrong assumptions about the radial incompleteness of the data set. To further test this result, we investigate a different completeness function that drops with distance from the Galactic plane (see Test 5, Example 2, in Table 3 and Figure 20). We get a similar robust behaviour for small deviations, and only slightly less robustness for larger deviations. That an explanation for this robustness could be, that much of the information about the potential comes from the rotation curve, which is not affected by incompleteness, is demonstrated in Figure 22.

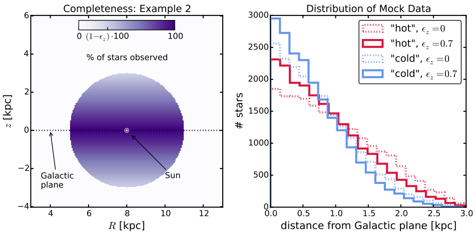

Figure 20. Selection function and mock data distribution for investigating vertical incompleteness of the data. All model parameters are summarized as Test 5, Example 2, in Table 3. The survey volume is a sphere around the sun and the percentage of observed stars is decreasing linearly with distance from the Galactic plane, as demonstrated in the left panel. How fast this detection/incompleteness rate drops is quantized by the factor ϵ_z. Histograms for four data sets, drawn from two MAPs (**`hot`** in red and **`cool`** in blue, see Table 2) and with two different ϵ_z, 0 and 0.7, are shown in the right panel for illustration purposes. [TO DO: Potential and/or population names in typewriter font]

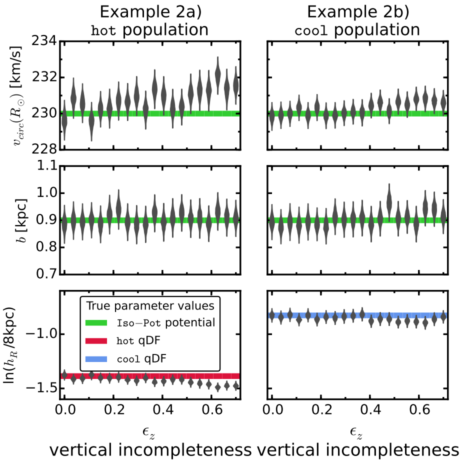

Figure 21. Influence of wrong assumptions about the incompleteness parallel to the Galactic plane of the data on the parameter reocovery with *RoadMapping*. Each mock data set was created having different incompleteness parameters ϵ_z (shown on the x-axis and illustrated in Figure 20) and the model parameters are given as Test 5, Example 2, in Table 3. The analysis however didn't know about the incompleteness and assumed that all data sets had constant completeness within the survey volume ($\epsilon_z = 0$). The marginalized likelihoods from the fits are shown as violins. The green lines mark the true potential parameters (`Iso-Pot`) and the red and blue lines the true qDF parameters (**`hot`** MAP in red and `cool` MAP in blue), which we tried to recover. The *RoadMapping* method seems to be robust against small to intermediate deviations between the true and the assumed vertical data incompleteness, as well as the radial incompleteness in Figure 21.

Marginalization over v_T.— The likelihood in Equation 11 is marginalized over the coordinate v_T as follows

$$\begin{aligned}
&\mathscr{L}(p_M \mid D)|_{(v_T\ \text{marg.})}\\
&= \prod_i^N P_{(v_T\ \text{marg.})}(\boldsymbol{x}_i, v_{R,i}, v_{z,i} \mid p_M)\\
&\equiv \prod_i^N v_0 \cdot \int_0^{1.5 v_{\text{circ}}(R_\odot)} \mathrm{d}v_T\ P(\boldsymbol{x}_i, v_{R,i}, v_T, v_{z,i} \mid p_M)
\end{aligned}$$

where $P(\boldsymbol{x}, \boldsymbol{v} \mid p_M)$ is the same as in Equation 11 and the numerical integral over v_T is performed as a 24th order Gauss-Legendre quadrature. The additional factor of v_0 is needed to get the units of $P_{(v_T\ \text{marg.})}(\boldsymbol{x}_i, v_{R,i}, v_{z,i} \mid p_M)$ right.

[TO DO: Mention in text or caption how the panels looked that I removed.]

REFERENCES

Batsleer, P., & Dejonghe, H. 1994, A&A, 287, 43

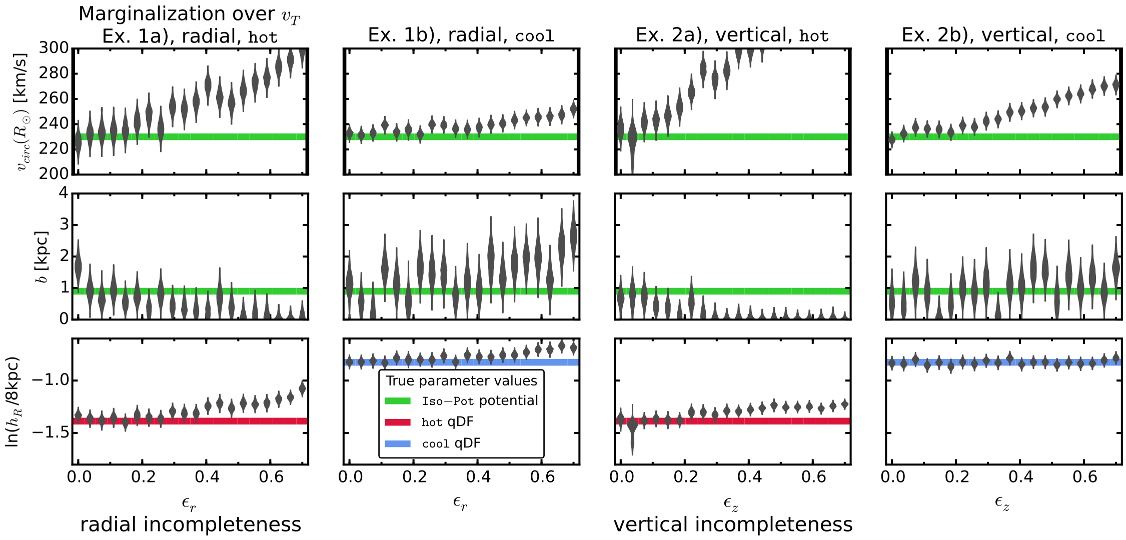

Figure 22. Influence of wrong assumptions about radial and vertical incompleteness on the parameter recovery, when *not* including information about the tangential velocities in the analysis. The mock data sets are the same as in Figure 9 and 21, but this time we did not include the data coordinates v_T in the analysis and therefore marginalized the likelihood over v_T instead (see §.1). This demonstrates that much of the information about the potential is actually stored in the rotation curve, i.e. $v_T(R)$, which is not affected by removing stars from the data set. But even if we do not include v_T we can still recover the potential within the errors, at least for small ($\epsilon_z \lesssim 10\%$).

Binney, J. 2010, MNRAS, 401, 2318

Binney, J., & McMillan, P. 2011, MNRAS, 413, 1889

Binney, J. 2011, Pramana, 77, 39

Binney, J. 2012, MNRAS, 426, 1324

Binney, J. 2012, MNRAS, 426, 1328

Binney, J. 2013, NAR [TO DO: emulateapj doesn't know NAR], 57, 29

Binney, J., & Tremaine, S. 2008, Galactic Dynamics: Second Edition, by James Binney and Scott Tremaine. ISBN 978-0-691-13026-2 (HB). Published by Princeton University Press, Princeton, NJ USA, 2008.

Bovy, J., & Tremaine, S. 2012, ApJ, 756, 89

Bovy, J., Rix, H.-W., & Hogg, D. W. 2012b, ApJ, 751, 131

Bovy, J., Rix, H.-W., Hogg, D. W. et al., 2012c, ApJ, 755,115

Bovy, J., Rix, H.-W., Liu, C., et al. 2012, ApJ, 753, 148

Bovy, J., & Rix, H.-W. 2013, ApJ, 779, 115

Bovy, J. 2015, ApJS, 216, 29

Büdenbender, A., van de Ven, G., & Watkins, L. L. 2015, MNRAS, 452, 956

Dehnen, W., & Binney, J. 1998, MNRAS, 294, 429

de Lorenzi, F., Debattista, V. P., Gerhard, O., & Sambhus, N. 2007, MNRAS, 376, 71

Famaey, B., & Dejonghe, H. 2003, MNRAS, 340, 752

Foreman-Mackey, D., Hogg, D. W., Lang, D., & Goodman, J. 2013, PASP, 125, 306

Garbari, S., Liu, C., Read, J. I., & Lake, G. 2012, MNRAS, 425, 1445

Gilmore, G., & Reid, N. 1983, MNRAS, 202, 1025

Henon, M. 1959, Annales d'Astrophysique, 22, 126

Holmberg, J., Nordström, B., & Andersen, J. 2009, A&A, 501, 941

Hunt, J. A. S., & Kawata, D. 2014, MNRAS, 443, 2112

Hunt, J. A. S., & Kawata, D. 2014, MNRAS, 443, 2112

Jurić, M., Ivezić, Ž., Brooks, A., et al. 2008, ApJ, 673, 864

Kawata, D., Hunt, J. A. S., Grand, R. J. J., Pasetto, S., & Cropper, M. 2014, MNRAS, 443, 2757

Klement, R., Fuchs, B., & Rix, H.-W. 2008, ApJ, 685, 261

Kuijken, K., & Gilmore, G. 1989, MNRAS, 239, 605

McMillan, P. J. 2011, MNRAS, 414, 2446

McMillan, P. J. 2012, European Physical Journal Web of Conferences, 19, 10002

McMillan, P. J., & Binney, J. J. 2008, MNRAS, 390, 429

McMillan, P. J., & Binney, J. 2012, MNRAS, 419, 2251

McMillan, P. J., & Binney, J. J. 2013, MNRAS, 433, 1411

Nordström, B., Mayor, M., Andersen, J., et al. 2004, A&A, 418, 989

Perryman, M. A. C., de Boer, K. S., Gilmore, G., et al. 2001, A&A, 369, 339

Piffl, T., Binney, J., McMillan, P. J., et al. 2014, MNRAS, 445, 3133

Read, J. I. 2014, Journal of Physics G Nuclear Physics, 41, 063101

Rix, H.-W., & Bovy, J. 2013, A&A Rev., 21, 61

Sanders, J. L., & Binney, J. 2015, MNRAS, 449, 3479

Sellwood, J. A. 2010, MNRAS, 409, 145

Steinmetz, M., Zwitter, T., Siebert, A., et al. 2006, AJ, 132, 1645

Strigari, L. E. 2013, Phys. Rep., 531, 1

Syer D., Tremaine S. 1996, MNRAS, 282, 223

Ting, Y.-S., Rix, H.-W., Bovy, J., & van de Ven, G. 2013, MNRAS, 434, 652

Yanny, B., Rockosi, C., Newberg, H. J., et al. 2009, AJ, 137, 4377

Zhang, L., Rix, H.-W., van de Ven, G., et al. 2013, ApJ, 772, 108

[TO DO: In which order should I give the references????]

[TO DO: replace the references which I typed myself with the ones from ADS.]

[TO DO: Check if all references are actually used in paper. ???]

Table 3
Summary of test suites in this work: The first column indicates the test suite, the second column the potential, DF and selection function model etc. used for the mock data creation, the third model the corresponding model assumed in the analysis, and the last column lists the figures belonging to the test suite. Parameters that are not left free in the analyis, are always fixed to their true value. Unless otherwise stated we calculate the likelihood by the nested-grid and MCMC approach outlined in §2.7 and use $N_x = 16$, $N_v = 24$, $n_\sigma = 5$ as numerical accuracy for the likelihood normalisation in Equations (11) and (9).

Test		Model for Mock Data	Model in Analysis	Figures
Test 1 :	*Potential:*	`KKS-Pot`	-	Mock data:
Influence of	*DF:*	`hot` or `cool` qDF		Figure 2
survey volume on	*Survey volume:*	a) $R \in [4, 12]$ kpc,$z \in [-4, 4]$ kpc, $\phi \in [-20°, 20°]$.		
mock data distribution,		b) $R \in [6, 10]$ kpc,$z \in [1, 5]$ kpc, $\phi \in [-20°, 20°]$.		
also in action space	*# stars per data set:*	20,000		
	# data sets:	4 (= 2 × 2 models)		
Test 2 :	*Potential:*	`Iso-Pot`, `MW13-Pot` & `KKS-Pot`	-	Convergence
Numerical accuracy	*DF:*	`hot` qDF		of normalisation:
in calculation	*Survey volume:*	sphere around sun, $r_\text{max} = 0.2, 1, 2, 3$ or 4 kpc		Figure 3
of the likelihood	*Numerical accuracy:*	$N_x \in [5, 20]$, $N_v \in [6, 40]$, $n_\sigma \in [3.5, 7]$		
normalisation				
Test 3.1 :	*Potential:*	`Iso-Pot`	`Iso-Pot`, all parameters free	Figure 4
pdf is a	*DF:*	`hot` qDF	qDF, all parameters free	
multivariate	*Survey Volume:*	sphere around sun, $r_\text{max} = 2$ kpc	(fixed & known)	
Gaussian	*# stars per data set:*	20,000		
for large data sets.	*# data sets:*	5 (only one is shown)		
	Numerical accuracy:		$N_v = 20$ and $n_\sigma = 4$	
Test 3.2 :	*Potential:*	`Iso-Pot`	`Iso-Pot`, free parameter: b	Figure 5
Width of the	*DF:*	`hot` qDF	`hot` qDF, free parameters:	
likelihood scales			$\ln\left(\frac{h_R}{8\text{kpc}}\right), \ln\left(\frac{\sigma_{R,0}}{230\text{km s}^{-1}}\right), \ln\left(\frac{h_{\sigma,R}}{8\text{kpc}}\right)$	
with number of stars	*Survey volume:*	sphere around sun, $r_\text{max} = 3$ kpc	(fixed & known)	
by $\propto 1/\sqrt{N}$.	*# stars per data set:*	between 100 and 40,000		
	# data sets:	132		
	Analysis method:		likelihood on grid	
	Numerical accuracy:		$N_v = 20$ and $n_\sigma = 4$ (for speed)	
Test 3.3 :	*Potential:*	2 `Iso-Pot` with	`Iso-Pot`, free parameter: b	Figure 6
Parameter estimates		$b = 0.8$ kpc or $b = 1.5$ kpc		
are unbiased.	*DF:*	`hot` or `cool` qDF	`hot`/`cool` qDF, free parameters:	
			$\ln\left(\frac{h_R}{8\text{kpc}}\right), \ln\left(\frac{\sigma_{R,0}}{230\text{km s}^{-1}}\right), \ln\left(\frac{h_{\sigma,R}}{8\text{kpc}}\right)$	
	Survey volume:	5 spheres around sun, $r_\text{max} = 0.2, 1, 2, 3$ or 4 kpc	(fixed & known)	
	# stars per data set:	20,000		
	# data sets:	640 (= 2 × 2 × 5 models ×32 realisations)		
	Analysis method:		likelihood on grid	
	Numerical accuracy:		$N_v = 20$ and $N_\sigma = 4$ (for speed)	
Test 4 :	*Potential:*	i) `Iso-Pot` or ii) `MW13-Pot`	i) `Iso-Pot`, all parameters free	Figure 7
Influence of			ii) `MW13-Pot`, R_d and f_h free	
position & shape	*DF:*	`hot` qDF	i) qDF, all parameters free	
of survey volume			ii) qDF, only h_R, $\sigma_{z,0}$ and $h_{\sigma,R}$ free	
on parameter recovery	*Survey volume:*	4 different wedges, see Figure 7, upper right panel	(fixed & known)	
	# of stars per data set:	20,000		
	Analysis method:		i) MCMC, ii) likelihood on grid	
Test 5 :	*Potential:*	`Iso-Pot`	`Iso-Pot`, all parameters free	Illustration & mock data:
Influence of	*DF:*	a) `hot` or b) `cool` qDF	qDF, all parameters free	Figures 8 & 20
wrong assumptions	*Survey volume:*	sphere around sun, $r_\text{max} = 3$ kpc	(fixed & known)	Analysis results:
about the data set	*Completeness:*	*Example 1:* radial incompleteness,	data set complete,	Figures 9 & 21
(in-)completeness		completeness(r) $= 1 - \epsilon_r \frac{r}{r_\text{max}}$, twenty $\epsilon_r \in [0, 0.7]$	completeness(r) $= 1$, $\epsilon_r = 0$	Analysis results:

Table 3 — *Continued*

Test		Model for Mock Data	Model in Analysis	Figures
on parameter recovery		$r \equiv$ distance from sun,		when not using v_T data:
		Example 2: planar incompleteness,	data set complete,	Figure 22
		completeness$(z) = 1 - \epsilon_z \frac{\lvert z\rvert}{r_{\max}}$, $\epsilon_r \in [0, 0.7]$,	completeness$(r) = 1$, twenty $\epsilon_z = 0$	
		$z \equiv$ distance from Gal. plane.		
	# stars per data set:	20,000		
	# data sets:	40 ($= 2 \times 2 \times 20$)		
Test 6.1 :	*Potential:*	`Iso-Pot`	”Iso-Pot, all parameters free”	Figure 10
Numerical convergence	*DF:*	`hot` qDF	qDF, all parameters free	
of convolution	*Survey Volume:*	sphere around sun, $r_{\max} = 3$ kpc	(fixed & known)	
with measurement	*Errors:*	δRA $= \delta$DEC $= \delta(m-M) = 0$	Convolution with	
errors		$\delta v_{\rm los} = 2$ km/s	perfectly known errors	
		$\delta\mu_{\rm RA} = \delta\mu_{\rm DEC} =$ 2,3,4 or 5 mas/yr		
	Numerical Accuracy:		convolution using MC integration	
			with between 25 and 1200 MC samples	
	# stars per data set:	10,000		
	# data sets:	16 ($= 4 \times 4$ realisations)		
Test 6.2 :	*Potential:*	`Iso-Pot`	`Iso-Pot`, all parameters free	Figure 11
Testing the	*DF:*	`hot` qDF	qDF, all parameters free	
convolution	*Survey Volume:*	sphere around sun, $r_{\max} = 3$ kpc	(fixed & known)	
with measurement & without	*Errors:*	δRA $= \delta$DEC $= 0$	Convolution with errors,	
errors with		$\delta v_{\rm los} = 2$ km/s	ignoring distance errors in position (see §2.6)	
distance errors		$\delta\mu_{\rm RA} = \delta\mu_{\rm DEC} =$ 1, 2,3,4 or 5 mas/yr		
		a) $\delta(m-M) = 0$, b) $\delta(m-M) \neq 0$ (see Figure 11)		
	Numerical Accuracy:		800 or 1200 MC samples	
	# stars per data set:	10,000		
	# data sets:	40 ($= 2 \times 5 \times 4$ realisations)		
Test 6.3 :	*Potential:*	`Iso-Pot`	`Iso-Pot`, all parameters free	Figure 13
Underestimation	*DF:*	`hot` or `cool` qDF	qDF, all parameters free	
of proper motion	*Survey volume:*	sphere around sun, $r_{\max} = 3$ kpc [TO DO: CHECK]	(fixed & known)	
errors	*Errors:*	only proper motion errors	Convolution with proper motion errors	
		1, 2 or 3 mas/yr	10% or 50% underestimated	
	# stars per data set:	10,000		
	# data sets:	24 ($= 2 \times 2 \times 3 \times 3$ realisations)		
Test 7 :	*Potential:*	`Iso-Pot`	`Iso-Pot`, all parameters free	mock data:
Deviations in the	*DF:*	mix of two qDFs	single qDF, all parameters free	Figure 14
assumed DF		*Example 1:* with fixed qDF parameters,		Analysis results:
from the		but 20 different mixing rates:		Figures 15 & 16
star's true DF		a) `hot` & `cooler` qDF or b) `cool` & `hotter` qDF		
		Example 2: 20 fixed 50/50 mixtures,		
		with varying qDF parameters (by X%):		
		a) `hot` & `colder` qDF or b) `cool` & `warmer` qDF		
	Survey volume:	sphere around sun, $r_{\max} = 2$ kpc	(fixed & known)	
	# stars per data set:	20,000		
	# data sets:	40 ($= 2 \times 2 \times 20$)		
Test 8 :	*Potential:*	`MW14-Pot`	`KKS-Pot`, all parameters free,	potential contours:
Deviations of the			only $v_{\rm circ}(R_\odot) = 230$km s^{-1} fixed	Figure 18
assumed potential model	*DF:*	`hot` or `cool` qDF	qDF, all parameters free	qDF recovery:
from the star's	*Survey volume:*	sphere around sun, $r_{\max} = 4$ kpc	(fixed & known)	Figure 19
true potential	*# stars per data set:*	20,000		
	# data sets:	2		

[TO DO: Remove # data sets, where it actually is not important.] [TO DO: Jo suggested to make many tables from this. But I actually like one big table at the end of the paper. Otherwise we had 6 additional tables interrupting the flow of text and figures all the time. And the parameters in the table are really just for reference.] [TO DO: Overall, this table could do with a little less information.]